Peer-reviewed version available at *Materials* **2018**, *11*, 440; doi:10.3390/ma11030440

Article

Optical aggregation of gold nanoparticles for SERS detection of proteins and toxins in liquid environment: towards ultrasensitive and selective detection

Antonino Foti [1,a], Cristiano D'Andrea [1,b], Valentina Villari [1], Norberto Micali [1], Maria Grazia Donato [1], Barbara Fazio[1], Onofrio M. Maragò [1], Raymond Gillibert [2], Marc Lamy de la Chapelle [2,3] and Pietro G. Gucciardi [1,*]

[1] CNR-IPCF, Istituto per i Processi Chimico-Fisici, Viale F. Stagno D'Alcontres 37, I-98168, Messina, Italy; foti@ipcf.cnr.it (A.F.); c.dandrea@ifac.cnr.it (C.D'A.); villari@ipcf.cnr.it (V.V.); micali@ipcf.cnr.it (N.M.); donato@ipcf.cnr.it (M.G.D.); fazio@ipcf.cnr.it (B.F.); onofrio.marago@cnr.it (O.M.M.)

[2] Laboratoire CSPBAT, Université de Paris 13, Sorbonne Paris Cité, CNRS, 74 Rue Marcel-Cachin, F-93017 Bobigny, France; marc.lamydelachapelle@univ-lemans.fr (M.L.); raymond_gillibert@yahoo.fr (R.G.)

[3] Institut des Molécules et Matériaux du Mans (IMMM - UMR CNRS 6283), Université du Mans, Avenue Olivier Messiaen, 72085 Le Mans, France;

* Correspondence: gucciardi@ipcf.cnr.it; Tel.: +39-090-39762-248

Abstract: Optical forces are used to aggregate plasmonic nanoparticles and create SERS-active hot spots in liquid. When biomolecules are added to the nanoparticles, high sensitivity SERS detection is accomplished. Here we tailor this methodology to detect catalase and hemoglobin, two Raman resonant biomolecules, at concentrations down to 10 nM and 1 pM. Subsequently, we study the SERS signal in Bovine Serum Albumin as a function of the concentration, finding a monotonic dependence that suggests the possibility of quantitative detection. Finally, by exploiting nanoparticles functionalized with specific aptamers, we obtain first results on the SERS detection of Ochratoxin A, a fungal toxin found in food commodities and wine. This represents a first step towards the addition of molecular specificity to this novel biosensor strategy.

Keywords: SERS; biosensor; gold nanoparticles; aptamers; toxins; hemeprotein; optical forces; optical tweezers; optical patterning; colloids.

1. Introduction

Surface enhanced Raman spectroscopy (SERS) [1, 2] has proven to be an extraordinary tool for direct (*label-free*) detection of biological entities and biomedical applications [3,4,5]. The huge amplification of the electric field provided by the resonant excitation of localized surface plasmons (LSP) [6,7] can bypass issues related to the low non-resonant Raman scattering cross-section of biomolecules in the visible range ($\sigma_{scatt} \sim 10^{-30}$ cm^{-2} molecule^{-1} sr^{-1}) [8]. The SERS effect can be an efficient transducer among the class of optical biosensors, giving access to the spectroscopic information, useful to get insight on the interactions of biomolecules with its environment and to know its structure and conformation [9,10]. Label-free SERS detection of proteins in liquid environment has the further advantage of keeping proteins in their natural habitat. Creation of SERS-active aggregates in a solution containing biomolecules, without affecting their functionality, is still a challenge [9]. Gold or silver colloidal solutions are the most suitable systems for in-liquid

a Now at LPICM, Ecole Polytechnique, CNRS, 91128 Palaiseau France

b Now at CNR - Istituto di Fisica Applicata "Nello Carrara" (IFAC), I-50019 Sesto Fiorentino (FI)

Peer-reviewed version available at Materials 2018, 11, 440; doi:10.3390/ma11030440

SERS detection, representing a three-dimensional matrix that closely interacts with the analytes in its native form when they are mixed together [11]. Individual nanoparticles (NPs) do not provide enough amplification for SERS detection of biomolecules. NPs clusters, conversely, can be extremely effective in accomplishing such a task [3,12]. When the gap between the NPs is below 10 nm, in fact, the SERS enhancement factor (*EF*) at the interstices of the nanostructures (*hot spots)* can increase by a factor 10 to 10^4, thanks to the rise of new gap plasmon resonances [1,13]. Obtaining a controlled aggregation of plasmonic colloids with analytes located in hot-spots is, therefore, a crucial point for the fabrication of a ultra-low sensitive SERS sensors working in liquid environment. Water in the interstices among the nanoparticles prevents the colloidal system from collapsing, and then causing a strong reduction of the *EF* [14] due to quantum plasmonics effects [15,16]. This allowed to reach attomolar molecular sensitivity [17,18], demonstrating that "wet" plasmonic aggregates can be more sensitive with respect to the dried ones. Simple ways to aggregate colloidal plasmonic nanoparticles involve the addition of external chemical agents, such as salts [19] or pyridine [20]. Such methodologies can provide very strong SERS amplification (~ 10^6 —10^{11}) [1] but also large signal instabilities and lack of reproducibility. Inducing the NPs aggregation *via* addition of acidified sulfate to the solution containing the target protein yields SERS-active colloid-protein complexes in which the biomolecules are located at the NPs hot spots [3]. With this strategy, quantitative detection of non-resonant proteins was achieved at concentrations down to 5 μg/mL on Lysozime (Lys). Chemicals can also be added to a protein solution mixed with NPs in order to create NP-protein-NP structures at the interface of an optical fiber immersed inside the sample pushing the sensitivity down to 0.2 μg/mL [4]. However an acidic environment (pH 3) is needed and this dramatically alters the natural configuration of the biomolecules. Iodide-modified Ag NPs (Ag IMNPs) [10] aggregate by protein addition, making the detection process more biocompatible. A limit of detection (LOD) of 3 μg/mL was achieved for Lys, and 300 μg/mL for Bovine Serum Albumin (BSA). Aggregation of NPs with biocompatible coatings is also a feasible way for SERS detection (LOD ~ 50 nM for cytochrome C) [21].

Photochemical and photophysical effects induced by light can trigger the formation of SERS-active structures for detection of chemical compounds in liquid [22,23,24]. Remote aggregation and SERS sensing can be achieved by using optical fibers [25]. Aggregation triggered by light irradiation can be reversible when it exploits thermophoretic effects [26] or temperature-responsive coil-to-globule transitions [27], induced by plasmonic heating [28]. The interaction between light and metal NPs is also mediated by optical forces [29,30]. They enable contactless manipulation, providing novel routes to achieve efficient SERS in-liquid [31,32], in a controlled and chemicals-free way [32,33], offering new strategies for single molecule detection [34] and *in-vivo* applications [35]. The nature of the light-particle interaction can be switched from the attractive (optical trapping) to the repulsive regime (optical pushing) [36] by changing the intensity or wavelength of the light beam. When the laser field is far-off the particle's LSPR, optical forces are dominated by the gradient force and can either attract or repel the metal NPs from the high field intensity regions [37,38]. When light is nearly-resonant to the NPs LSPR, conversely, the radiation pressure prevails and metal NPs are pushed along the beam axis [35,39,40].

Svedberg et al. first showed the possibility to create SERS-active dimers by optical manipulation of metal NPs in liquid, showing SERS signals of organic molecules dissolved therein [41]. This experiment paved the way to new strategies for SERS detection in liquid [42,43] and lab-on-chip microfluidic architectures [44,45] *via* optical manipulation of colloids, with sensitivities that can reach the fM range for simple molecules. We recently applied optically induced aggregation of gold nanorods to the SERS detection of aminoacids and proteins (BSA, Lys) in liquid (LIQUISOR) with sensitivity down to 100 nM in concentration, showing the potential of this technique in the field of biomolecular sensing [46].

An ideal biosensor besides being highly sensitive must also feature high specificity and capability of quantitative determination of the amount of the target molecule in solutions. Raman is indeed a quantitative technique. Although SERS suffers from signal variability issues due to the heterogeneity of the hot spots distribution and molecular binding, a proper statistical sampling and

advanced data analysis [3] can be used to obtain concentration information [47,48,49]. Highly specific SERS detection of analytes in complex environments, like body fluids, can be implemented by functionalizing the NPs with bioreceptors such as antibodies or aptamers [50,51,52] i.e. grabbing strategies routinely employed in well assessed indirect biosensors like quartz crystal microbalance (QCM), enzyme-linked immunosorbent assays (ELISA) and surface plasmon resonance (SPR) [53,54,55]. Thiolated aptamers are DNA strands designed to interact with specific kinds of molecules, on one side, and with gold surfaces on the other. Thiolated aptamers have gained much favor in SERS biosensing because they stably link to gold NPs and because their small dimension (20-100 unit bases) permits to keep the target molecules in the hot spot of the NPs, thus taking advantage of the local enhanced field [56,57,58].

The aim of this article is to show that LIQUISOR is capable of ultrahigh sensitivity on resonant Raman biomolecules and to provide first results towards quantitative proteins detection and specific toxins detection using aptamer-functionalized NPs. In the first part we study the dynamics of the aggregation process. We develop a model describing the relations between analyte concentration and the measured SERS signal that supports the experimental findings. In the second part we show that Catalase (Cat) and Hemoglobin (Hgb), two Raman resonant biomolecules important for oxygen transport, biological defense and regulation of oxidation processes in living organisms, can be detected with LIQUISOR at concentration down to 10 nM (Cat) and 1 pM (Hgb). Finally, we show that nanorods functionalized with specific aptamers are effective to capture target molecules of Ochratoxin A (OTA), a fungal toxin occurring in food commodities and wine, paving the way towards highly specific LIQUISOR applications.

2. Materials and methods

2.1. Gold Nanorods

We use gold nanorods from Nanopartz (35 nm diameter × 90 nm length and 30 nm diameter × 50 nm length), dispersed in deionized (DI) water at a concentration of 0.05 mg/ml; the solution contains <0.1% ascorbic acid and <0.1% Cetyltrimethylammonium bromide (CTAB) surfactant to prevent re-aggregation. The solution pH varies between 3 and 4. The rods have a positive ζ-potential (+40 mV). Major plasmon resonances are at 690 nm (35x90) and at 540 nm (30x50).

2.2 Glass microcell

As microcells we employ microscope glass slides with single cavities (15 – 18 mm dia., 0.5 – 0.8 mm depth, Marienfled GmbH), sealed with standard 170 μm-thick glass coverslips (Forlab). They can accommodate up to 75 μL of NRs-biomolecules solution. Smaller amounts (15 μL) can be analyzed with custom-built microcells, made with a bi-adhesive spacer 120 μm thick attached on a glass slide and sealed with a glass coverslip. All the glasses are washed by immersion in a deionized watery solution (1% v/v) of HELLMANEX III detergent for 10-15 min, followed by rinsing in DI water in order to remove the residual detergent. Finally they are washed with ethanol and dried in air.

2.3 Protein solutions

BSA, Hgb and Cat are purchased from Aldrich in lyophilized powder state and diluted in Phosphate Buffered Solution (PBS, pH 7.2). PBS solutions 200 mM are prepared by dissolving Na_2HPO_4 (14.94 g) and NaH_2PO_4 (5.06 g) in 200 mL of DI water. BSA is diluted in PBS (200 mM) at concentrations ranging from 10^{-3} to 10^{-8} M, and then mixed with nanorods (both families) in a 7:1 v/v volume ratio. Hgb (10^{-4} – 10^{-12} M) and Cat (10^{-5} – 10^{-8} M) are diluted in PBS 10 mM, and then mixed with the nanorods (30 nm diameter × 50 nm length) in a volume ratio 4:1 v/v. Solutions are prepared in 1.5 mL Eppendorfs from which 80 μL aliquots are pipetted into the glass microcells. All the solutions are prepared and used at room temperature.

2.4 Gold nanorods functionalization

Aptamers for OTA are thiolated single strand DNA (ssDNA) and were purchased from Eurogentec. They are composed by 36 nucleotides (M_w ~ 11.5 kDa) and have the following specific sequence: 5′-HS-$(CH_2)_6$- GAT CGG GTG TGG GTG GCG TAA AGG GAG CAT CGG ACA-3′. This sequence was determined by Cruz-Aguado and Penner [59] and it was already used by B. Galarreta et al. for SERS detection of OTA with a limit of detection of 50 nM [57]. NRs are functionalized with the DNA aptamers with the following protocol. The NRs (30 nm diameter × 50 nm length) are diluted in DI water in a volume ratio of 1:4 v/v. Aptamers are diluted in PBS 10 mM down to a concentration of 1 μM and then mixed with the NRs solution in a volume ratio of 1:3 v/v. NRs are let incubate with aptamers for 1h.

2.5 Toxin solutions preparation

Ochratoxin A was purchased from Sigma Aldrich in powder state and was diluted in PBS 10 mM at the final concentration of 1 μM and mixed with the functionalized NRs in a volume ratio of 3:1 v/v. The system is let incubate for 2h at room temperature.

2.6 Dynamic Light Scattering

Dynamic light scattering (DLS) [60] has been exploited to obtain dimensional information, namely the mean hydrodynamic radius (MHR), of BSA-nanoparticles' complexes in liquid solutions. DLS experiments are carried out with a Photon Correlation Spectroscopy setup. A He–Ne laser source (10 mW), polarized orthogonal to the scattering plane, is focused onto the sample and the scattered light is collected at 90° by using a self-beating detection mode. Two photomultipliers are used for light detection, in a pseudo-cross correlation mode at the same scattering angle. For collection of the polarized and depolarized scattered light, a Glan-Thomson analyzer is placed in the scattered beam. During the experiment each sample is put in a glass cuvette positioned inside a thermostat in order to perform the experiment in a thermal equilibrium condition.

2.7 Extinction spectroscopy

Extinction spectroscopy has been used to study the aggregation properties of the BSA-NRs complexes by monitoring their time- and concentration- dependent plasmon resonances. Extinction spectra are acquired using the internal white light source embedded in the XploRA microspectrometer (Horiba Jobin Yvon) for excitation. Collection of the light transmitted through the microcell containing the NRs-protein solution is performed with a 10X microscope objective (Olympus M-Plan, NA 0.2) [61]. Detection of the transmitted intensity (I_T) is accomplished with a Peltier cooled CCD (Sincerity). We consider here the absorbance profile to assign the plasmon resonance, calculated as $-\log_{10}(I_T/I_0)$, where I_0 is the excitation intensity. For these experiments NRs –BSA solutions are prepared in a 1 mL eppendorf and 80 μL aliquotes are pipetted to the glass microcell for analysis at defined time intervals.

2.8 Raman spectroscopy setups

LIQUISOR has been operated on different confocal Micro-Raman Spectrometers: a LabRam HR800, a XploRA and a XploRA PLUS (Horiba Jobin Yvon). The HR800 employs a He-Ne laser source (λ = 632.8 nm); the beam is focused by means of a 100X microscope objective (Olympus M-Plan, NA = 0.90, WD = 210 μm) on a ~600nm diameter spot. The laser power on the sample is 5 mW, enough to apply a sufficient radiation pressure on the nanorods for process activation. Optical aggregation has also been accomplished with long working distance microscope objectives (Olympus LMPlanFl 50X, NA 0.5, WD = 10.6 mm; Olympus LUCPLFLN 60X, NA 0.7, WD = 1.5 mm), as long as we use higher laser power (13 – 18 mW). For these experiments an XploRA and an XploRA PLUS setup are used, with laser diode sources at 660 nm and 638 nm, respectively. In all the cases, the SERS signal is collected via the same illumination objective, in backscattering, dispersed by a 600 l/mm grating and detected through a Peltier-cooled silicon CCD (Synapse and Sincerity by

Peer-reviewed version available at *Materials* **2018**, *11*, 440; doi:10.3390/ma11030440

Horiba Jobin Yvon or Andor iDus DU 420). Spectra are acquired with integration times from seconds to tens of seconds.

3. Results and Discussion

3.1. LIQUISOR operation

The working principle of the LIQUISOR [46] is illustrated in Figure 1a. CTAB-coated gold NRs are added to a solution of biomolecules dissolved in PBS. Molecular interactions (see sect. 3.2) yield the formation of biomolecule-NRs complexes (BIO-NRCs) in solution (inset in Figure 1a). This latter is pipetted into a glass microcell and positioned under the Raman micro-spectrometer, where it is irradiated with a laser beam focused by a microscope objective.

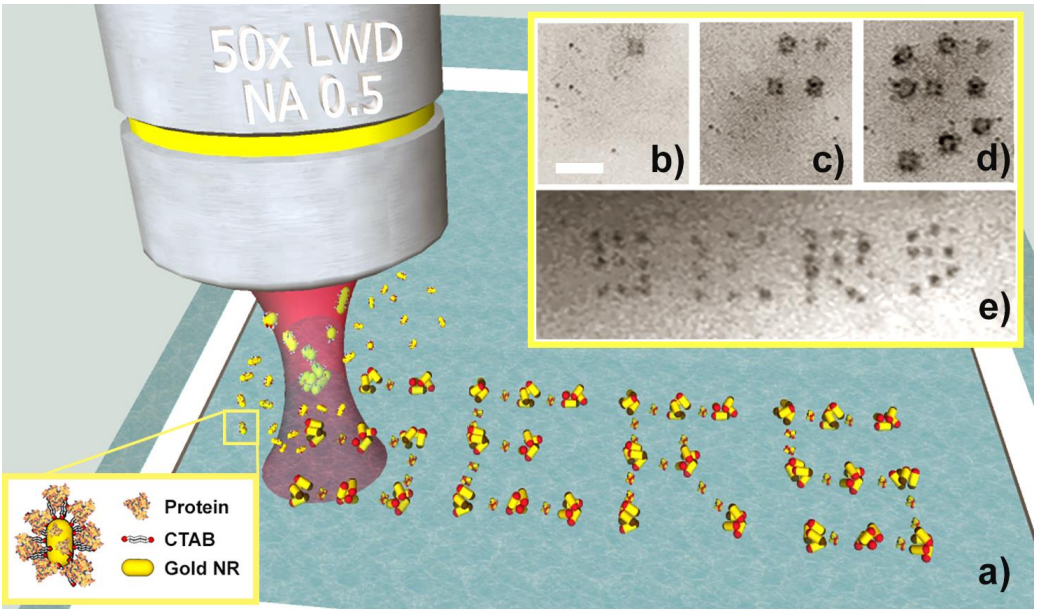

Figure 1: (a) Sketch of the LIQUISOR methodology in which a focused laser beam optically aggregates BIO-NRCs complexes (inset). (b-d) Optical pictures of BIO-NRCs aggregates produced sequentially to print the word "SERS" (e) in liquid. Scale bar is 15 μm.

In our experiments we use 30x50 nm NRs featuring a single plasmon resonance at 540 nm (Supplementary Figure S1, blue line) and 35x90 nm NRs featuring a short axis resonance at 520 nm (Supplementary Figure S1, green line) and a more intense long axis resonance at 690 nm. In both NRs families the optomechanical interaction with the laser beams (λ = 633, 638, 660 nm) is dominated by the scattering force, no matter if the field is polarized parallel to the short or to the long axis of the NRs (see calculations in ref. [46] for the 35x90 nm NRs and in Supplementary Figure S2 for the 30x50 nm ones). Positioning the laser spot close to the bottom of the microcell, the BIO-NRCs intercepted by the laser beam are pushed from the focal point towards the microcell surface where they stick and aggregate. It is therefore possible to aggregate the BIO-NRCs in a confined region having dimensions in the 5 – 10 μm range (black spot in Figure 1b) on time scales ranging from few to some tens of minutes. By displacing the laser spot with a micro- or a nano-positioning stage, it is possible to print optically on the glass microcell controlled patterns of BIO-NRCs in a sequential way (Figure 1c-e). Due to the rod-rod near-field interaction, the aggregates feature very strong field enhancement effects, yielding an intense SERS emission from the biomolecules located inside the *hot spot* regions. In Figure 2 we compare (a) a conventional Raman spectrum of BSA at 1 mM (the minimum detectable concentration in PBS), with the SERS signal of BSA in PBS at 50 nM, a concentration 20,000 times smaller, acquired by the LIQUISOR technique (b). The SERS signal shows strong contributions in the regions of the Phe ring breathing (1004 cm^{-1}), to the amide III (1237 cm^{-1}) and to the COO^- vibration (see ref. [46] for more details on the modes

Preprints (www.preprints.org) | NOT PEER-REVIEWED | Posted: 19 January 2018 doi:10.20944/preprints201801.0181.v1

Peer-reviewed version available at Materials 2018, 11, 440; doi:10.3390/ma11030440

attribution). Notably, in those regions, the CTAB signal detected from NRs precipitated in PBS in absence of the protein (c), does not provide any contribution, excluding signal cross-talk. The positioning of the laser focus close to the bottom of the microcell is critical. No aggregation or SERS signal is observed when the laser spot is focused into the solution.

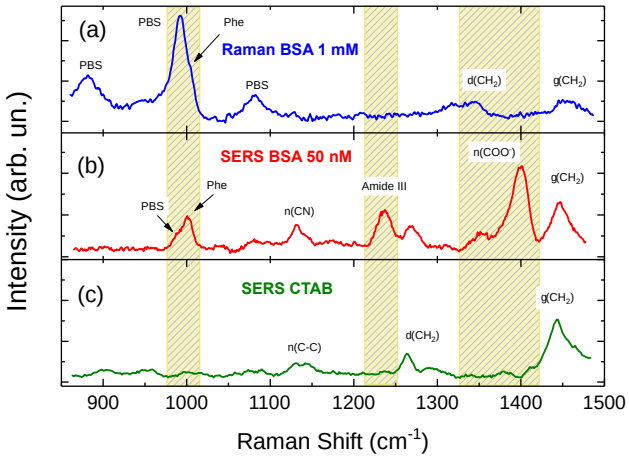

Figure 2: (a) Raman spectrum of BSA 1 mM in PBS. (c) SERS spectrum of BSA 50 nM in PBS. (c) SERS signal detected on NRs precipitated in absence of protein, attributed to the residual CTAB.

3.2. NRs-Biomolecules interactions in buffered solutions

Upon mixing, the biomolecules bind to the gold NRs [62]. Due to the interplay between the electrostatic interaction of molecules surrounding the NRs with the positively charged CTAB bilayer and the destabilization of the CTAB bilayer induced by the PBS at physiological pH, amino acid residues of the protein get in close contact with NRs gold surface [63,64,65,66]. This yields the formation of biomolecule-NRs complexes [65,67] in which individual NRs are stabilized by the protein layer in the solution. The formation of the BIO-NRCs was studied on BSA, which is a protein rich of sulfur spread over 17 disulfides (S-S), 5 methionine ($S\text{-}CH_3$) and one free thiol (a cysteine residue) [65]. Disulfide bridges contribute to a stable protein tertiary structure as they give solidity the α-helix bundles. When they interact with gold nanoparticles, the high sulfur affinity with gold causes the disruption of the S-S bridges and the fast creation of the Au-S coordination [68]. As a result, the protein forms a corona all-around the gold nanostructure changing its tertiary structure [65]. Stable colloidal suspensions are obtained if the protein quantity is sufficient to recover the surface and prevent attractive interaction causing precipitation [65]. This is also the case of NRs covered with CTAB. When we mix BSA (10^{-4} M) in PBS (200 mM in water), the high ionic concentration and the pH value of 7.2 causes the destabilization of the CTAB bilayer surrounding the NRs [63]. The presence of BSA and its fast interaction with the gold surface (they form a stable bound in less than 1 μs [65]) ensures a new protein capping layer that can stabilize the suspension.

In order to get insight on the concentration dependence of the SERS signal in the LIQUISOR experiments, we have first studied the BSA-NRs complexes' size as a function of the protein amount. We use DLS to measure the mean hydrodynamic radius of the complexes in the 0.1 mM – 50 nM concentration range. In this range BSA cannot be detected by conventional Raman, whereas strong SERS is found using the LIQUISOR approach [46]. BSA molecules in PBS at 0.1 mM have a mean hydrodynamic radius (MHR) r_0 ~ 6 nm at room temperature [46]. The scattering is almost totally polarized indicating that BSA is in the folded conformation. Upon addition of gold NRs (30x50) the MHR increases to $r_0 = (60 \pm 10)$ nm (Figure 3a, red symbols). This value is ca. 2.5 times the MHR of the pristine CTAB-coated NRs (Figure 3a, purple line). The size is constant over all our observation period (270 min), indicating that the BIO-NRCs, after a very fast uptake of BSA from the solution, are stabilized. A different behavior is observed at lower BSA concentrations. At 10 μM, 5 μM and 1 μM, the size of the complexes grows with time (blue, green, orange symbols in Figure 3a), reaching a

Preprints (www.preprints.org) | NOT PEER-REVIEWED | Posted: 19 January 2018 doi:10.20944/preprints201801.0181.v1

Peer-reviewed version available at Materials 2018, 11, 440; doi:10.3390/ma11030440

steady state after some minutes. Fitting the data with a simple growth model $r(t) = r_0 + A(1 - e^{-t/t_0})$, with r_0 the initial MHR, A the size increase and t_0 the process timescale, we find that the stabilization of the BIO-NRCs dimensions takes few minutes at 10 μM ($t_0 = 5 \pm 3$ min) and ca. 10 minutes ($t_0 = 11 \pm 3$ min) at 5 μM. At 1 μM the process is slower ($t_0 = 45 \pm 20$ min). In addition, larger complexes are obtained at 1 μM: the MHR (200 nm) almost doubles with respect to the complexes obtained at 10 μM (90 nm) and triples with respect to ones at 100 μM (60 nm). At the lowest concentrations (100 and 50 nM, purple and brown symbols in Figure 3a) the MHR of the BIO-NRCs keeps increasing. A stable configuration is never reached within our maximum observation period (270 min). In this ranges, data are well fitted with a power law model $r(t) \sim t^b$, with $b = 0{,}23 \pm 0{,}01$ for both concentrations (pink and brown lines). In Figure 3b we plot the size of the complexes Vs BSA concentration at four different time intervals, i.e. soon after mixing (2 min, pink triangles), in a time scale typical of the LIQUISOR experiments (20 – 60 min, blue circles and green triangles) and in a timescale (270 min, red triangles) larger that the longest LIQUISOR acquisitions (typically 60 – 120 min). 2 min after mixing the complexes have MHR between 60 and 75 nm (error is between 5 and 10 nm). After 20 minutes the size is unchanged (60 ± 10 nm) at 100 μM, while it increases to values between 90 ± 10 nm (10 μM) and 140 ± 20 nm (1 μM and lower concentrations).

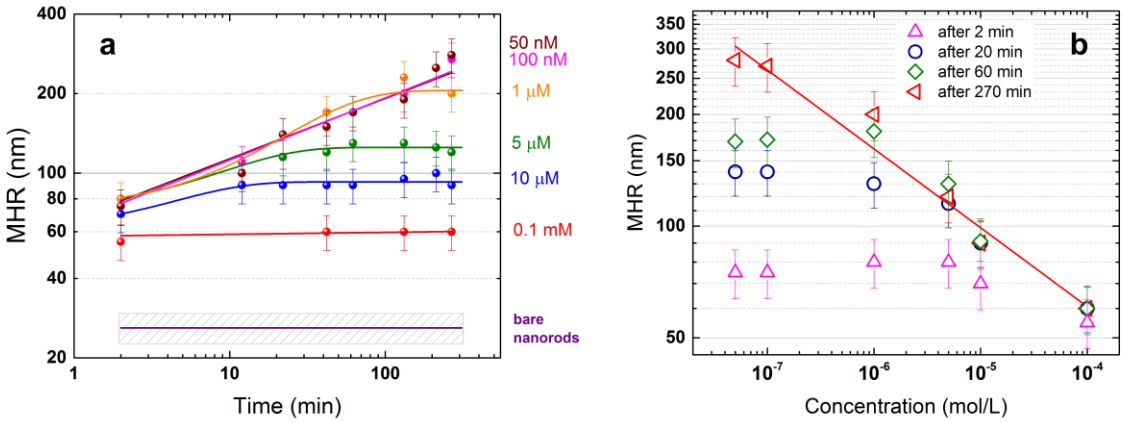

Figure 3 – (a) Mean hydrodynamic radius (MHR) of BIO-NRCs as a function of time at BSA concentrations of 0.1 mM (red dots), 10 μM (blue dots), 5 μM (green dots), 1 μM (orange dots), 100 nM (pink dots) and 50 nM (brown dots). The solid colored lines are fits of the experimental data using a model $r(t) = r_0 + A(1 - e^{-t/t_0})$. Best fit parameters are: $r_0 = 70 \pm 20$ nm, $A = 140 \pm 20$ nm, $t_0 = 45 \pm 20$ min (orange line – 1 μM); $r_0 = 72 \pm 7$ nm, $A = 53 \pm 7$ nm, $t_0 = 11 \pm 3$ min (green line – 5 μM); $r_0 = 60 \pm 10$ nm, $A = 35 \pm 10$ nm, $t_0 = 5 \pm 3$ min (blue line – 10 μM). The purple line represents the MHR measured on the CTAB-coated pristine NRs. Data at 100 and 50 nM are fitted with a power law $r(t) \sim t^b$ with $b = 0{,}23 \pm 0{,}01$ for both concentrations (pink and brown lines). (b) MHR as a function of protein concentration after 2 min (pink triangles), 20 min (blue circles), 60 min (green diamonds) and 270 min (red triangles) from the mixing. (red line) Power law fit of the data. Best fit exponent -0.21 ± 0.02.

After 270 min the complexes formed below 1 μM have further increased their dimension to 200 ± 30 nm (1 μM), 260 ± 30 nm (100 nM) and 270 ± 30 nm (50 nM), whereas at higher concentrations (5 μM, 10 μM and 100 μM) no appreciable size increase is observed. Fitting the data with a power law $r(c) \sim c^b$ (red line in Figure 3b), we find an exponent value of -0.21 ± 0.02. This power law also holds on time scales between 20 and 60 min at concentrations of 1 – 100 μM. We find, finally, that the scattering intensity is stable for concentrations down to 5 μM, while a continuous decrease of the signal is observed with time for lower concentrations. The scattering intensity decrease at 90° is, indeed, expected due to precipitation of nanoparticles, but could also be due to a change in the form factor which is difficult to predict given the uncertainty of the nanostructure shape.

Peer-reviewed version available at Materials 2018, 11, 440; doi:10.3390/ma11030440

Extinction spectroscopy becomes crucial at this stage to understand the nature of the growing objects in solution. To this aim we have studied the plasmon resonance of the complexes formed on time scales and protein concentrations relevant for the LIQUISOR operation (from few minutes to some hours and from 100 μM to 50 nM). In Figure 4a (dark yellow line) we show the resonance profile of the NRs diluted in water compared with the ones obtained after mixing with BSA in PBS (colored lines). Within the first 3 minutes from the mixing, the resonance red shifts and broaden. At 100 μM (red line) the shift is limited to some nm and the resonance profile is still well fitted by a single peak (Supplementary Figure S3a, green dots and blue curve). This suggests that a large number of individual NRs populate the solution. Considering that the dimension observed at this concentration is ~ 60 nm, we probably have the formation of a protein multilayer around the NRs surface. Decreasing the concentration, the resonance remarkably red shifts and broadens (Figure 4a blue, green, orange, magenta, brown lines), likely due to coupling effects among NRs that form aggregates very rapidly (few minutes or less) [46, 69]. We phenomenologically describe the resonance profiles of such a system with a two components Gaussian, one peaked ~ 540 nm and a second one red-shifted and broadened. Such a model fits well the data at all concentrations (see Supplementary Figure S3b). Measurements as a function of time show that the LSPR properties of the complexes are strongly concentration-dependent. In Figure 4b we plot the position of the second, red shifted peak as a function of time, finding a behavior that closely resembles the one observed in the DLS measurements (Figure 3a). At 100 μM (red squares) the resonance wavelength is almost constant, suggesting that the protein quantity is enough to stabilize the NRs at the single nanoparticle level. At 10 μM (blue circles), after an initial slight red-shift of the resonance, we observe a steady state and a final blue shift (on time scales exceeding 100 min). This behavior is more pronounced at 5 μM (green triangles), with an initial red-shift of the resonance and a final blue shift. NRs aggregates between 90 and 150 nm are present in the solution at these concentrations, stabilized by an external protein layer. Very likely, a smaller number of NRs, not fully covered by the protein, form unstable aggregates that precipitate at times larger than 100 min, leaving in the solution only smaller objects. This can justify both the fictitious blue shift effect observed in the LSPR profiles and the slight MHR decrease (although within the error bar) observed at 5 and 10 μM (Figure 3a).

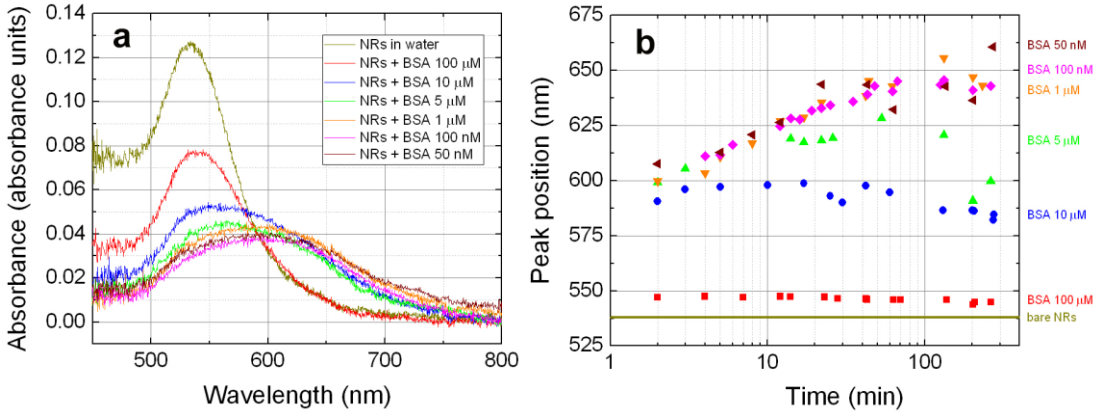

Figure 4: (a) Plasmon resonance of the NRs diluted in water (gold line) and after few minutes from mixing with BSA in PBS at different concentrations. (b) Position of the red-shifted component of the plasmon resonance of the BSA-NRs complexes as a function of time for different BSA concentrations. In all the fits the position of the 540 nm peak (not shown) is constant within ±3%.

At lower concentrations (1 μM to 50 nM) the red-shift is continuous with time (orange, magenta and brown symbols) and rather independent from the specific concentration. Some saturation is observed only on time scales exceeding 100 min. At these concentrations the quantity of protein is insufficient to stabilize the complexes. Larger and larger NRs aggregates (MHR > 200 nm) are formed in the solution, which precipitate on longer time scales. Similarly to what observed in the scattering intensity at 90°, here the integrated absorbance is almost constant down to 5 μM and starts

decreasing with time at lower concentrations, supporting the occurrence of precipitation phenomena. Spectra acquired after 1 day (data not shown), in fact, show that at 1 μM and below the absorbance is almost zero confirming that the quasi totality of the NRs aggregates is precipitated, whereas of stable LSPR fingerprints are found at concentrations of 5 μM and higher.

On the time scales relevant for LIQUISOR operation (5 – 100 min) we can conclude that the BIO-NRCs solution is mainly composed by individual NRs at 100 μM and by NRs aggregates at 10 and 5 μM, both stabilized by a protein corona. At lower concentrations (1 μM down to 50 nM) we have larger and larger NRs aggregates with a protein surface coverage insufficient to stabilize them. Notably, the plasmon resonance peak is always close to the laser wavelength, ensuring that the scattering force is always prevalent, giving rise to optical forces that push the BIO-NRCs along the beam propagation direction at any concentration and time.

Our experiments suggest a picture in which three concurrent processes contribute to the formation of the BIO-NRCs: (i) the destabilizing effect of the PBS that causes aggregation of the NRs with a consequent size increase and red-shift of the plasmon resonance; (ii) the surface coverage of the protein that replaces the CTAB and stabilizes the NRs to some steady dimensions and plasmon resonance wavelengths; (iii) the precipitation of aggregates not fully stabilized by the protein, yielding the fictitious blue shift of the LSPR observed on the longest time scales. At high concentration, BSA is enough to cover the surface of the NRs almost immediately, stabilizing the colloids and avoiding any relevant aggregation. As we decrease the concentration in the micromolar range, the probability for the analyte to bind to the NRs surface is smaller [70], and then the time necessary to totally cover and stabilize the BIO-NRCs increases. In the meanwhile the PBS keeps on destabilizing the CTAB micellar capping, leading to the aggregation of NRs before the formation of a stabilizing protein corona. BSA, having several accessible sulfurs on its surface, can also act as a bridge between different nanorods also fostering the aggregates formation. Aggregates that are not fully stabilized by the protein form larger structures that do precipitate. At the lowest concentrations (1 μM – 50 nM) the quantity of protein is insufficient to cover the BIO-NRCs surface, provoking a continuous size increase of the aggregates, a process that ends up with precipitation of the structures.

3.3. SERS intensity Vs concentration

In ref. [46] we have already shown that at 100 μM, the rise of the SERS signal occurs through several steps: (i) the onset of the process in which first aggregates form on the cell walls and yield some detectable SERS signals (this phase takes from few tens of seconds to some minutes from the beginning of the irradiation); (ii) a stabilization phase which produces a stronger, well distinct, SERS signal (taking place on time scales of few tens of seconds); (iii) a repeated increase of the aggregate size (minutes, tens of minutes) due to the capture of further BIO-NRCs, with a continuous growth of the SERS signal; (iv) a saturation (several tens of minutes, up to one hundred minutes) in which the BIO-NRCs have totally filled up the laser focus and the SERS signal becomes constant. Here we analyze the SERS dynamics at decreasing BSA concentrations. We acquire spectra at regular intervals under laser irradiation and focus the attention on the time dependence of the Phe peak intensity at 1004 cm^{-1} [46]. To assess the reproducibility of the SERS signal, for each concentration we analyze at least 4 different aggregates. A first analysis is carried out on the saturation time, i.e. the time elapsed from the activation of the process (first detectable signal) to the full saturation of the signal. In Figure 5 (black circles) we observe that decreasing the protein concentration, *c*, the SERS signal takes less time to saturate,[c] following a power law dependence with exponent 0.26 ± 0.01 in the range from 0.1 μM to 100 μM (red line in Figure 5). This behavior can be understood on the basis of the DLS and LSPR measurements, as discussed below, and is confirmed by the simple hydrodynamic model described in sect. 3.4.

---

c - Note that the saturation time is different from the time interval needed to trigger the aggregation process which, instead, generally increases when decreasing the concentration.

Preprints (www.preprints.org) | NOT PEER-REVIEWED | Posted: 19 January 2018 doi:10.20944/preprints201801.0181.v1

Peer-reviewed version available at Materials 2018, 11, 440; doi:10.3390/ma11030440

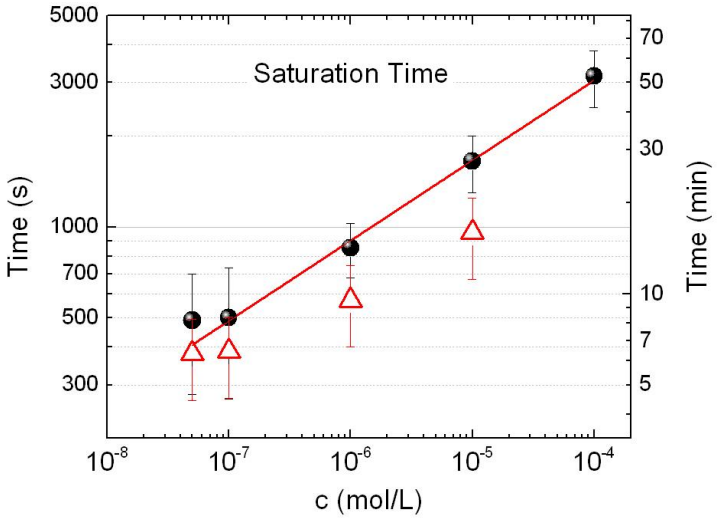

Figure 5 – Saturation time (black dots) plotted against BSA concentration. Each point is the average of the saturation times for at least three different aggregates. Red line is power law fit with exponent 0.26 ± 0.01 (best fit parameter). Red symbols are estimated values for T_{sat} from the hydrodynamic model (Eq. 6).

Figure 6a displays the time evolution of the SERS signal for each concentration as a function of the irradiation time, starting form the activation of the process. It highlights how the LIQUISOR dynamics is qualitatively similar for each concentration, with an onset, a phase of signal increase and a final saturation. The SERS signal increases in a step-like fashion at the onset, while during the intermediate phase it shows a continuous increment. The signal growth is slow at the beginning; it becomes faster after some hundreds of seconds (when the growth rate reaches its maximum), and then slows down again approaching saturation. The SERS intensity curves in the intermediate phase of the process are well fitted with a Boltzmann growth kinetics equation [34] (solid lines in Figure 6a), given by:

$$I = \frac{I_0 - I_{\text{sat}}}{1 + e^{(t-t_0)/dt}} + I_{\text{sat}}, \quad (1)$$

where I_0, I_{sat} define the initial and final (saturation) value of the SERS intensity I. t_0 is the time at which I reaches half of its saturation value and also represents the time at which the signal growth rate (curve slope) is maximum. The quantity $v = (I_{\text{sat}} - I_0)/4dt$ measures the curve slope at t_0 and, therefore, corresponds to the maximum velocity of the SERS signal growth. From the physical point of view, v can be considered as the speed at which the hot spots are created, which is related to the nanoparticles aggregation rate in the laser spot. From the fitting of the curves we retrieve the values of v and I_{sat} as a function of the concentration, plotted respectively in the inset of Figure 6a (black symbols) and in Figure 6b (black symbols). Both v and I_{sat} increase as a function of the protein concentration with a power law dependence featuring exponents 0.40 ± 0.04 and 0.60 ± 0.04, respectively (red lines in inset of Figure 6a and Figure 6b are the result of the fits). The same trend (Supplementary Figure S4) is observed analyzing other distinctive BSA spectral features, i.e. the Amide III (1240, 1275 cm^{-1}) and Phe+Tyr modes (1585–1620 cm^{-1}), supporting the idea that the BSA configuration in the interaction with the NRs surface does not change with the protein concentration.

Preprints (www.preprints.org) | NOT PEER-REVIEWED | Posted: 19 January 2018 doi:10.20944/preprints201801.0181.v1

Peer-reviewed version available at Materials 2018, 11, 440; doi:10.3390/ma11030440

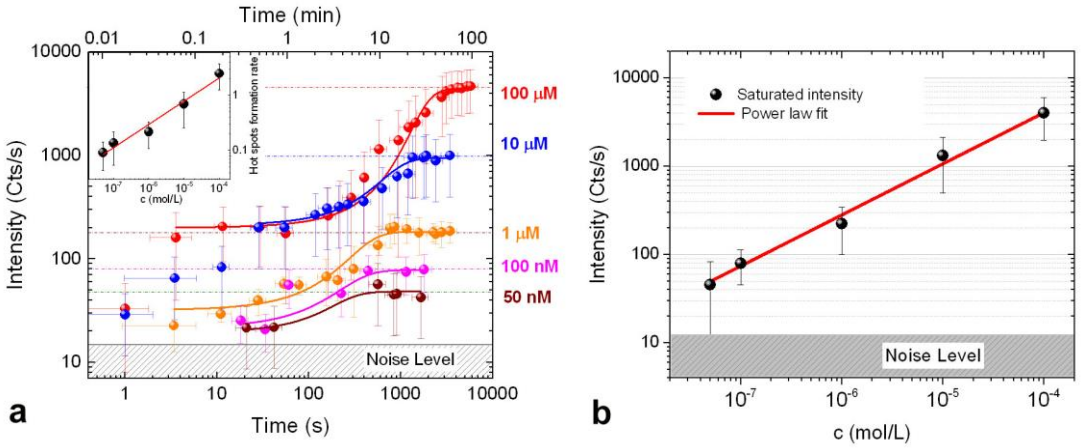

Figure 6 – (a) Time evolution of the SERS intensity at different BSA concentrations (colored dots). The time $T_0 = 0$ is set at the onset of the process, when the first weak SERS signal is detected (real-time observation). Starting from T_0 the signal is recorded at intervals corresponding to the integration time used in each spectrum. Solid lines are fits of data using a Boltzmann growth kinetics equation. (inset) Plot of the maximum signal growth rate vs BSA concentration. The solid red line is a power law fit with an exponent 0.40 ± 0.04 as best fit parameter. (b) Plot of the SERS intensity at saturation Vs BSA concentration (symbols). The red line is a power law fit with exponent 0.60 ± 0.04.

The experimental results can be interpreted, at least qualitatively, making some simple considerations on the origin of the SERS signal. Indeed, the SERS effect is triggered by the field enhancement provided by hot spots in plasmonic nanoparticles. Optical aggregation of 2D layered materials in presence of BSA at 100 μM, in fact, does not provide any Raman fingerprint of the protein [71], indicating that the mere accumulation of protein molecules in the focal spot, brought-in by the nanostructures, is not is not sufficient to provide a detectable signal. The SERS intensity measured at time t will scale with the number of hot spots present in the focal spot volume. Saturation of the SERS signal is achieved when the laser focus volume is filled with BIO-NRCs. From DLS we know that at lower BSA concentrations the size of the BIO-NRCs in solution is larger. Therefore, a smaller number of BIO-NRCs will be sufficient to saturate the laser focal volume. If we assume that the number of hot spots created in the focal region is proportional to the number of BIO-NRCs optically pushed independently from their size, the lower SERS intensity at saturation observed when decreasing the BSA concentration will be a direct consequence of the reduced number of hot spots. This hypothesis can also justify the fact that the saturation condition is reached more rapidly at lower concentrations (Figure 5), since filling the laser spot volume with a smaller number of larger BIO-NRCs will require less time. We can derive a simple physical model out of this picture. We call I_{sat} the saturated SERS signal, N_{NP}^{sat} the number of nanoparticles present at saturation in the focal spot volume V_{las}, R_H the MHR of the nanoparticles, V_{NP} the average particle's volume and, finally, N_{HS} the number of hot spots. From the considerations made above, we assume that $I_{sat} \propto N_{HS}$ and $N_{HS} \propto N_{NP}^{sat}$. From simple geometrical considerations, the number of structures in the focal volume is given by the volumes ratio $N_{NP}^{sat} \propto V_{las}/V_{NP}$. The volume of a nanostructure can be calculated from its hydrodynamic ratio as $V_{NP} \propto R_H^3$. Therefore we expect

$$I_{sat} \propto N_{NP}^{sat} \propto R_H^{-3} \quad (2)$$

Assuming the asymptotic concentration dependence of the MHR, $R_H \propto c^{-0.2}$, found by DLS (Figure 3b) we obtain

$$I_{sat} \propto c^{0.6} \quad (3)$$

in agreement with the experimental data (Figure 6b). Notably, such a steep dependence permits to distinguish BSA at different concentrations in a broad range, from 50 nM to 100 μM, in spite of the large signal fluctuations observed (up to 40%). Moreover, this monotonic dependence of the SERS

signal from the concentration opens up new possibilities to perform quantitative detection with the LIQUISOR methodology.

For what concerns the time needed to saturate the SERS intensity, we expect that T_{sat} is proportional to the number of hot spots present at saturation in the focal area, N_{HS}, and inversely proportional to the velocity at which the hot spots are created, v_{HS}. Again, if we assume $N_{HS} \propto N_{NP}^{sat} \propto c^{0.6}$ and take for v_{HS} the velocity of the SERS signal growth determined experimentally (see inset of Figure 6a), $v \propto c^{0.4}$, we find

$$T_{sat} \propto N_{NP}^{sat}/v \propto c^{0.2} \quad (4)$$

This trend is close to what found by fitting the experimental data, $T_{sat} \propto c^{0.26}$ [Figure 5(red line)]. A more detailed description of this aspect is developed in the next section.

A final comment regards the way in which the hot spots are formed in the LIQUISOR and how this affects the limit of detection. With BSA at 100 μM, the stability of the dispersion, the single-particle resonance profile of the BIO-NRCs in solution and the LSPR broadening observed upon aggregation [46], let us to conclude that the hot spots are, indeed, induced optically, with an interplay between pushing and thermal effects. At lower concentrations the solutions are populated with clusters of NRs spontaneously formed with proteins distributed on their surface. We expect that some of these are "hot clusters," i.e. SERS-active structures with protein molecules embedded in the hot spots [72]. In order to observe a strong SERS signal, however, we need to induce some optical aggregation. Focusing the laser in the liquid solution, e.g. at the center of the microcell, in fact, does not produce any detectable signal, at any concentration, suggesting that either the number of "hot clusters" in the solution is not relevant or that their SERS enhancement is not large enough. Furthermore, SERS spectra acquired on micron-sized structures spontaneously formed by precipitation after few hours from the mixing of NRs with BSA at 100 nM show no signal in most of the cases. Sometimes a SERS activity is observed, comparable to the one of early stage aggregates created by LIQUISOR, but the signal does not substantially increase with time. At this stage we do not have a final answer to the question whether the SERS signal at the lowest concentrations originates from an optical accumulation of "hot clusters," or if it is the consequence of new, more efficient hot spots created by the combination of optical pushing and thermally-induced effects in the laser focus. The measurements reported above, however, show unambiguously that aggregates produced optically are much more "SERS efficient" than those precipitated spontaneously, suggesting that the signal observed in the LIQUISOR is not a mere sum of the contribution of BSA-NRs aggregates spontaneously formed in the solutions. At concentrations of 10 nM we do not observe any SERS signal on the usual observation time scales, indicating that aggregation and precipitation takes place on much faster time scales than the protein uptake by the NRs. Under these experimental conditions the LOD is therefore estimated between 10 and 50 nM.

3.4. Hydrodynamic model of the aggregation process

We assume that the rate of laser volume filling depends on the diffusion coefficient D of the BIO-NRCs which, in turn, is related to the probability of entering in the laser beam, and on the speed at which these objects can reach the bottom of the glass microcell. The value of this speed is the equilibrium velocity that we can retrieve from the balance of forces acting on the nanostructure: the radiation force (F_{rad}), the gravity (F_g) and the buoyancy (F_b) forces and the drag force (F_{drag}). The contribution of these forces is illustrated in Figure 7.

Preprints (www.preprints.org) | NOT PEER-REVIEWED | Posted: 19 January 2018 doi:10.20944/preprints201801.0181.v1

Peer-reviewed version available at Materials 2018, 11, 440; doi:10.3390/ma11030440

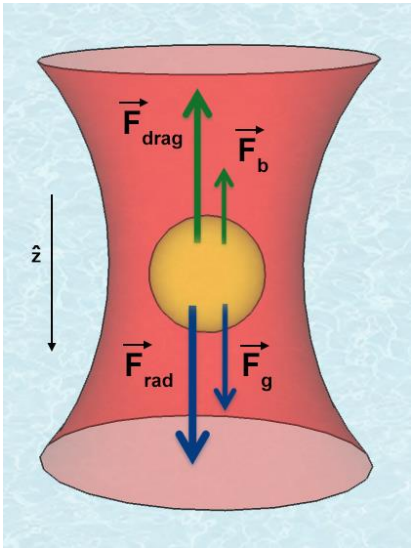

Figure 7 - Schematics illustrating all the forces acting on BIO-NRC, approximated here as a sphere. The drag ($\mathbf{F}_{drag}$) and the buoyancy ($\mathbf{F}_b$) force slow down the sphere motion, which is due to the radiation ($\mathbf{F}_{rad}$) and gravity ($\mathbf{F}_g$) force.

Considering the BIO-NRCs as nanospheres with radius equal to MHR, we can use the information retrieved from DLS measurements to model the trend of the saturation time as a function of the concentration. First of all we have to find the dependence of the filling rate (v_{fill}) on the MHR. The diffusion coefficient is given by the fluctuation-dissipation theorem [30]:

$$D = \frac{k_B T}{\gamma}, \tag{5}$$

where $\gamma = 6\pi\eta R_H$ is the Stokes' particle friction coefficient for a spherical particle of radius R_H. Therefore we have $D \propto R_H^{-1}$. On the other hand the force balance equation leads to:

$$F_{rad} + (F_g - F_b) = F_{drag}. \tag{6}$$

Using the Stokes law for the calculation of the drag force on a nanospheres with radius R_H, we have:

$$F_{drag} = \gamma v_{eq} = 6\pi\eta R_H v_{eq}. \tag{7}$$

Considering that F_{rad} is directly proportional to the nanoparticle polarizability α, which is proportional to the volume $V \propto R_H^3$, we have that $F_{rad} \propto R_H^3$, while for $(F_g - F_b)$ is given by:

$$(F_g - F_b) = (\rho_p - \rho_m)gV \propto R_H^3, \tag{8}$$

where ρ_p and ρ_m are the density of the particle and of the medium respectively. Therefore we can say that the left part in Eq. 6 is proportional to the cube of R_H and combining the result with Eq. 7, we can assert:

$$v_{eq} \propto R_H^2, \tag{9}$$

and finally we have that the rate of nanostructures filling the laser volume is related to the product of the diffusion coefficient and the equilibrium velocity:

$$v_{fill} \propto D v_{eq} \propto R_H. \tag{10}$$

The average experimental v_{fill} can be estimated by the ratio between the number of BIO-NRCs (N_{Nano}) necessary to fill the diffraction limited volume probed by the microscope objective (V_{laser}) and the measured saturation time (T_{sat}). V_{laser} can be estimated calculating the volume of Point

Spread Function (PSF) [73] of a TEM_{00} laser beam at wavelength λ, focused in air by an objective with numerical aperture NA. The PSF is well approximated by a prolate ellipsoid having semi-axes $b_1 = b_2 = 0.61 \times \lambda/NA$ and $b_3 = 2 \times \lambda/NA^2$, where b_3 is the semi-axis in the light propagation direction. The volume of the focused laser spot, therefore, will be $V_{laser} = (4\pi/3)b_1b_2b_3 \sim 2\lambda^3/NA^4$. For $\lambda = 633$ nm and $NA = 0.9$, we find $V_{laser} \sim 1.2$ μm³. On the other hand, N_{Nano} can be estimated in the ideal situation in which we consider a saturated aggregate where the NRs, surrounded by a protein bilayer, are closely packed and totally fill the focal laser spot. Thus N_{Nano} is given by the ratio between V_{laser} and the volume of one BIO-NRC, whose volume is approximated to $V_{BIO-NRC} = 4\pi/3\, R_H^3$.

Mixing NRs with BSA 0.1 mM leads to stable BIO-NRCs with R_H equal to 65 nm and the observed averaged saturation time for SERS intensity is $T_{sat}^{0.1\mathrm{mM}} = 3200 \pm 660$ s. Using these values we can estimate the number of nanostructures in the laser spot after saturation ($N_{Nano}^{0.1\mathrm{mM}} \sim 10^3$) and rate of filling $v_{fill} \sim 0.33 \pm 0.07$ nanostructures/s. Exploiting Eq. 7 we can rescale this value for lower concentrations taking into account the trends for R_H extrapolated from DLS measurements reported in Figure 3. Considering the operational time for LIQUISOR starting from 120s (the time necessary to prepare the sample and put it under the spectrometer), we can calculate the saturation time at 10 μM, 1 μM, 100 nM and 50 nM with the rescaled v_{fill} for each concentration. Values obtained from the model for the laser spot filling (red triangles in Figure 5) are quite in agreement with the observed values (black dots in Figure 5). The discrepancy between experimental and calculated values has to be ascribed to a combination of different issues: (i) the spherical approximation for the BIO-NRCs shape; (ii) the laser-induced heating of the NRs, which fosters the nanoparticles gathering and the protein uptake, this enlarging the dimensions of BIO-NRCs [46]; (iii) the dependence of the diffusion coefficient on the density n of diffusing BIO-NRCs. Indeed even if the initial concentration of NR mixed to protein solutions is kept constant, we saw the different dynamics of BIO-NRCs at different concentration leads to nanostructures of increasing dimensions as the concentration is lowered and as a result the density of diffusing objects decrease. This means that the model described above overestimates v_{fill} providing a shorter saturation time for SERS intensity with respect to the actual one, that is what we observe in Figure 5.

3.5. LIQUISOR detection of hemeproteins

Hemeproteins are characterized by the presence of the *heme* group, in which an iron atom is coordinated to 4 pyrrole nitrogens of protoporphyrin IX and to a imidazole nitrogen of a histidine residue from the globin side of the porphyrin [74]. This group allows the protein to accomplish several important tasks in biological systems, including oxygen transport, electron transfer as well as biological defense and regulation of oxidation mechanisms.

3.5.1. Hemoglobin

Hemoglobin (Hgb) is a globular metallo-protein composed of two α and two β subunits non-covalently bound. Each subunit chain is bound to one *heme* group. Raman spectroscopy can discriminate the normal conformational structure from pathological ones [75], based on the vibrational information on the heme group which is Raman-resonant under visible excitation [76]. SERS is capable of single molecule detection of Hgb [77]. However, in-liquid environment, SERS detection is more complicated and the sensitivity limited to ~ 100 nM [3,10].

We have carried out LIQUISOR detection of Hgb by laser irradiation of complexes obtained by mixing Hgb solutions in PBS with CTAB-capped gold NR (30 × 50 nm) resonant at 540nm (Supplementary Figure 1, blue line). Calculations of the optical forces acting on these NRs at 638nm with a 50X (NA 0.5) objective highlight (Supplementary Figure S2) the predominance of the scattering component over the gradient one. The NRs are, therefore, pushed by the laser beam, as confirmed by the experiment. The PBS concentration has been reduced to 10 mM because we observed unstable complexes and precipitation phenomena at 200 mM. In these new conditions the CTAB layer is stable on a longer timescale. Hgb, negatively charged, is attracted by the positively charged CTAB bilayer, permitting the formation of complexes also at ultralow concentration, where

Preprints (www.preprints.org) | NOT PEER-REVIEWED | Posted: 19 January 2018 doi:10.20944/preprints201801.0181.v1

Peer-reviewed version available at Materials 2018, 11, 440; doi:10.3390/ma11030440

the uptake of target molecules requires more time. Hemoglobin is diluted at concentrations down to 1 pM and the solutions are incubated with NRs (4:1 v/v) for three hours before measurements. Optical aggregation is induced by focusing the laser spot at about 5 μm from the surface of the glass microcell. Laser power is set between 6.5 and 23 mW, depending on the concentration. Once the BIO-NRCs start to aggregate and the first SERS signals is detected, the power is reduced to 3 mW whenever photo-induced damages to the protein are observed (i.e. with the appearance of amorphous carbon bands). Raman spectra of Hgb in both solution (0.1 mM and 10 μM) and powder state have been acquired for reference (Figure 8a,b).

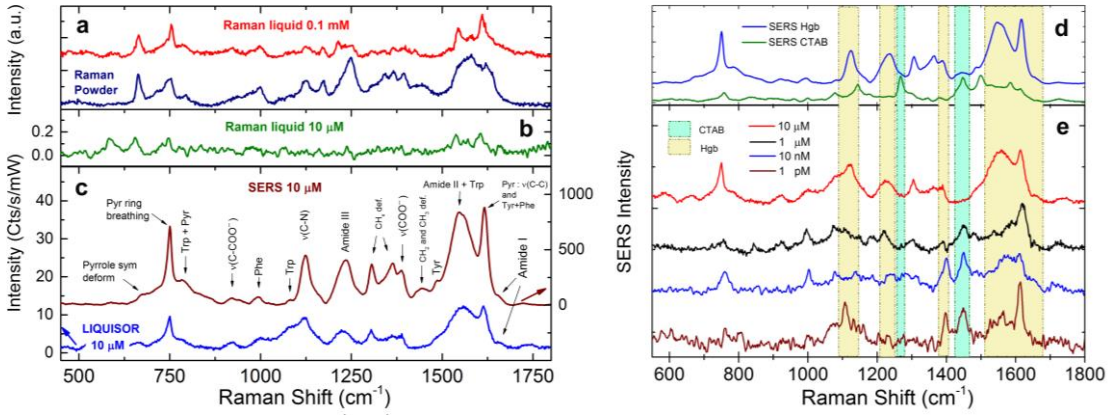

Figure 8 – (a) Raman spectra of Hgb 0.1 mM in PBS (red line – P = 18 mW, T = 60 s, 2 accumulations) and in powder state (blue line – P = 0.27 mW, T = 60 s, 5 accumulations). (b) Raman spectrum of Hgb 10 μM in PBS (P = 18 mW, T = 240 s, 2 accumulations). (c) SERS spectra of Hgb 10 μM acquired with the LIQUISOR methodology (blue line, P = 6.5 mW, T = 1 s) and on a spontaneous aggregate formed after 24h incubation (brown line – P = 3 mW, T = 1s). (d) Reference SERS spectra from aggregates for Hgb (blue line) and CTAB (green line – P = 6.5 mW, T = 1s, 120 accumulations). (e) SERS spectra of Hgb at decreasing concentrations (P = 6.5 mW, T = 1s, 50 accumulations). Yellow boxes highlight SERS bands due to the protein while green boxes are due to the CTAB SERS peaks.

They show the most important vibrational bands of Hgb at 664 cm^{-1} (pyrrole bending), 750 cm^{-1} (pyrrole breathing), 1125 cm^{-1} (CN and CC stretching), 1235 cm^{-1} (amide III), 1393 cm^{-1} (COO^- stretching), 1543 cm^{-1} (Amide II + Trp), 1585 – 1620 cm^{-1} (Phe + Tyr, CC stretching), 1655 cm^{-1} (Amide I) [75,76,78]. A more detailed list with assignment of the SERS bands of Hgb is reported in Supplementary Table S2. At 10 μM we find the Raman limit of detection of Hgb in PBS (Figure 8b, spectrum acquired with 18 mW of laser power and 240 s of integration). At the same concentration, the LIQUISOR methodology permits to detect a clear SERS fingerprint of Hgb after few minutes of irradiation, with 1s integration and 6.5 mW of incident power (Figure 8c, blue line). This corresponds to a net signal gain of ~ 10^2, considering the modes at in the 1500 – 1660 cm^{-1}. The spectral features well compare with the reference Raman, as well with the SERS signal recorded on aggregates spontaneously precipitated after an incubation time of 24h (Figure 8c, brown line). In this case SERS signal gains are ~ 10^4 (note that this value is an underestimation of the SERS enhancement factor, whose calculation requires estimation of the number of probed molecules). The SERS of Hgb is definitely different from the signal detected on the precipitated aggregates of NRs without protein (Figure 8d, green line) that we attribute to the CTAB capping agent. Decreasing the concentration of Hgb we are able to optically induce SERS aggregates at 1 μM (Figure 8e, black line), 10 nM (blue line), down to 1 pM (brown line). The spectral shape of the amide II (1550 cm^{-1}) with the presence of the amide III band (1232 cm^{-1}) and C-N stretching modes at 1125 cm^{-1} (highlighted in yellow) give evidence of protein SERS detection even at the lowest concentrations. Another important marker for Hgb detection is the peak at around 1615 cm^{-1}, clearly visible also at 1 pM, which is due to the presence of Pyrrole rings of the heme groups included in the protein [78]. Moreover the SERS signal at 1395 cm^{-1}, attributed to the stretching vibration of the COO^- group confirms the electrostatic nature of the interaction between proteins and the CTA^+ heads covering the NRs surface [79]. Note

that, as the protein concentration decreases, the bands at 1268 and 1442 cm^{-1} due to CH_2 wagging and scissoring of the CTAB chains [80] (highlighted by the cyan boxes) appear and get stronger. The residual CTAB signal probably arises from the fact that some surfactant is still attached on the NRs surface. Finally the different amplification of Hgb bands at the different concentration is likely due to the fact that Hgb does not bind to the gold surface with the same configuration [81], therefore showing different groups to the gold surface. The poor protein quantity at the lowest concentrations prevents a statistical sampling of the whole configurations ensemble, resulting in a different intensity ratio of the protein peaks. A signal gain between 10^8 and 10^9 is found comparing the SERS intensity at 1 pM of the band at 1617 cm^{-1} due to the C-C stretching of the Pyrrole rings in the heme group with the Raman signal at 10 μM.

3.5.2. Catalase

Catalase (Cat) is an important enzyme for aerobic living organisms that catalyzes the decomposition of hydrogen peroxide to molecular oxygen and water [82]. Cat levels in living organisms can be related to the risk of liver cancer [83] or can be used to monitor the toxic effects of chemical pollutants in marine organisms [84]. SERS permits ultralow detection of Cat in liquid exploiting the chemical aggregation of silver nanoparticles with a LOD of 0.2 nM [3].

As for Hgb, Cat was diluted in PBS (10 mM). The reference Raman spectrum shown in Figure 9a is acquired on a Cat solution at concentration of 10 μM. The most intense vibrational modes of the protein are the C-O stretching of Tyrosinate-iron group at 1244 cm^{-1}, the CH scissoring modes of the vinyl in heme group at 1305 cm^{-1}, the pyrrole rings vibrations of the heme group at 1373 cm^{-1} (half ring symmetric stretching), the symmetric stretching of the group COO^- at 1390 cm^{-1}, the CH_2 CH_3 scissoring modes at 1452 cm^{-1} and Amide I band at 1650 cm^{-1}. Finally the band from 1550 to 1620 cm^{-1} is due to the aromatic aminoacids (Trp, Phe, Tyr) and to the pyrrole rings (C=C strecting at 1612-1620 cm^{-1}) [3,85]. No Raman signal is detected at 1 μM, suggesting that the LOD of Cat is between 1 and 10 μM. LIQUISOR measurements on Catalase at 10 μM are carried out by mixing the protein solution (in PBS 10 mM) with gold NRs (LSPR 540 nm) 4:1 v/v. The SERS spectrum (Figure 9c, green line) displays an enhancement of the most relevant modes of Cat observed in Raman (highlighted by yellow bands). The same holds for the measurement at 10 nM (blue line in Figure 9c), which represents the minimum concentration detected, and which shows spectral features distinct from the CTAB signal acquired on precipitated NRs in absence of protein (Figure 9b).

Preprints (www.preprints.org) | NOT PEER-REVIEWED | Posted: 19 January 2018 doi:10.20944/preprints201801.0181.v1

Peer-reviewed version available at Materials 2018, 11, 440; doi:10.3390/ma11030440

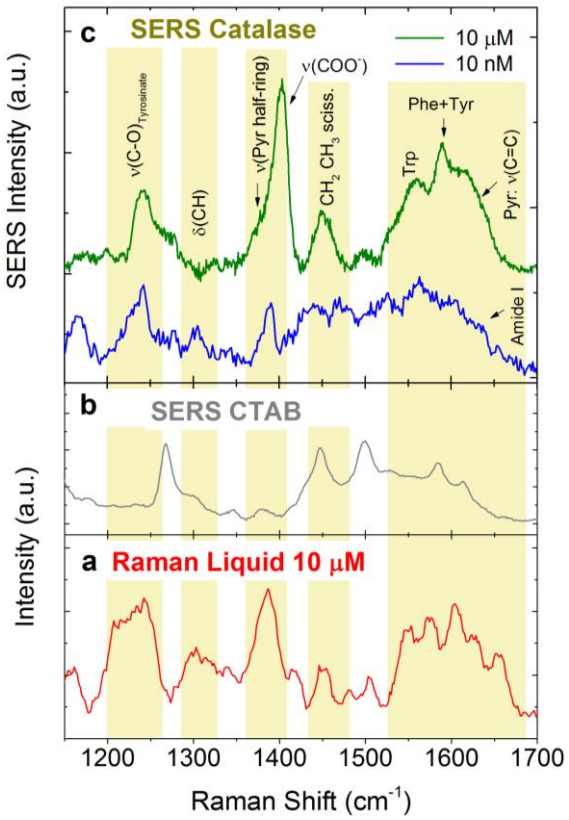

Figure 9 – (a) Raman spectrum in liquid of Catalase diluted at 10 μM in PBS 10 mM (P = 18 mW, T = 240s, 5 accumulations). (b) SERS spectrum of CTAB (grey line – P = 6.5 mW, T = 1s, 120 accumulations) (c) SERS spectrum of Catalase acquired with the LIQUISOR methodology at 10 μM (green line, T =1 s P = 3.5 mW, 30 accumulations) and 10 nM (blue line, T =1s P = 6.5 mW, 30 accumulations). Yellow boxes highlight the vibrational modes due to the protein.

3.6. LIQUISOR detection of ochratoxin A mediated by aptamers

Ochratoxin A is a nephrotic mycotoxin that can be found in different food products, such as cereals, wine, or coffee beans [86,87], representing potential public health risks. The maximum permissible concentration is in the range of 3–5 μg/kg, with a virtual safe dose for humans of less than 0.2 ng/kg per day for renal cancer risk [88]. Aptamer-based SERS sensors have been demonstrated for OTA identification down to 0.1 nM, employing Raman-active reporters [89] or at the concentration of 10 pM with the help of no labels [90], in dry conditions. Implementing the LIQUISOR methodology with the high selectivity of DNA aptamers can open interesting routes for ultra-low contactless specific SERS detection in liquid environment. Here we carry out first experiments to show that aptamer-functionalized nanoparticles can be used with the LIQUISOR to capture and detect OTA at micromolar concentration.

The strategy we follow is based on the following steps:

1. Functionalization of the gold NRs with bioreceptors through the substitution of the CTAB layer with thiolated aptamers. This is obtained during incubation of CTAB-coated NRs with aptamers in a PBS solution (10 mM). PBS destabilizes the CTAB, fostering the interaction between the NRs and the thiol groups of the aptamers.
2. Incubation of the functionalized NRs with the target molecules. Upon incubation the bioreceptors on the NRs surface will selectively capture the target proteins in the solution, creating BIO-NRCs surrounded by double layer including to the aptamers and the captured protein.
3. Normal operation of the LIQUISOR procedure (λ = 660 nm, Objective 60X, NA 0.7). Laser irradiation will produce aggregates in which the target molecules located at the hot spots will

Preprints (www.preprints.org) | NOT PEER-REVIEWED | Posted: 19 January 2018 doi:10.20944/preprints201801.0181.v1

Peer-reviewed version available at Materials 2018, 11, 440; doi:10.3390/ma11030440

experience an enhanced Raman scattering. This latter signal will show up, and compared to the SERS contribution from the aptamers.

Due to the high affinity between the thiol group of the ssDNA and the gold surface of NRs, the functionalization process takes advantage of the "one-pot" ligand exchange mechanisms [91], that enables the substitution of the stabilizing molecules (CTAB) with thiolated DNA aptamers (Figure 10c), which is more effective in correspondence of high curvature areas of NRs surface, where the CTAB bilayer has a lower density and ligand exchange processes are energetically more favorable with respect to the side zone of the NRs [91,92].

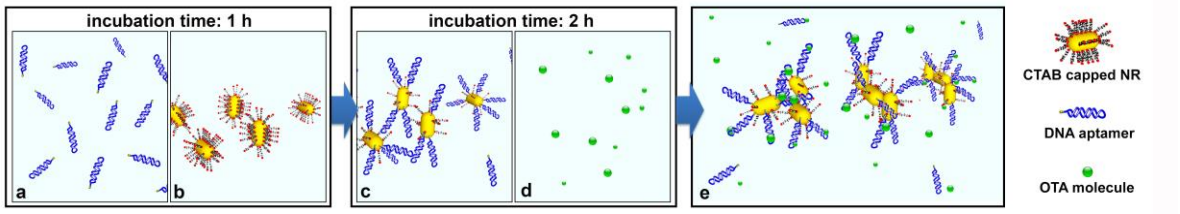

Figure 10 – Functionalization process. (a) ssDNA aptamer solution is mixed with (b) gold NRs in the volume proportion 1:3. After the system has incubated for 1 hour (c) the aptamer functionalized NRs are mixed with (d) the target molecules (OTA) in the volume proportion 3:1. The system is left in incubation for about 2 hours in order to allow the interaction between DNA aptamers and molecules for the formation of (e) the NR complexes.

The functionalization of gold CTAB-coated NRs with aptamers and their binding with OTA has been monitored by extinction spectroscopy. Interaction between NRs and molecules is evident looking at the LSPR time evolution of the mixture (Figure 11a). Very little shift (2 nm, stable with time) is caused by the aptamers (red lines), while a progressive LSPR red-shift and broadening is clearly observed when adding OTA (colored solid lines). A second contribution at higher wavelengths grows with time, while the peak at 537 nm is decreasing. In order to verify the success of the functionalization process, we compare the NRs signal with the ssDNA SERS coming from the optically induced aggregates made with functionalized NRs (Figure 11b). The ssDNA signal is consistent with the one reported in ref [57], and confirms a predominance of the vibrational modes due to guanine [57], and spectrally different from the background CTAB contribution (Figure 11c)

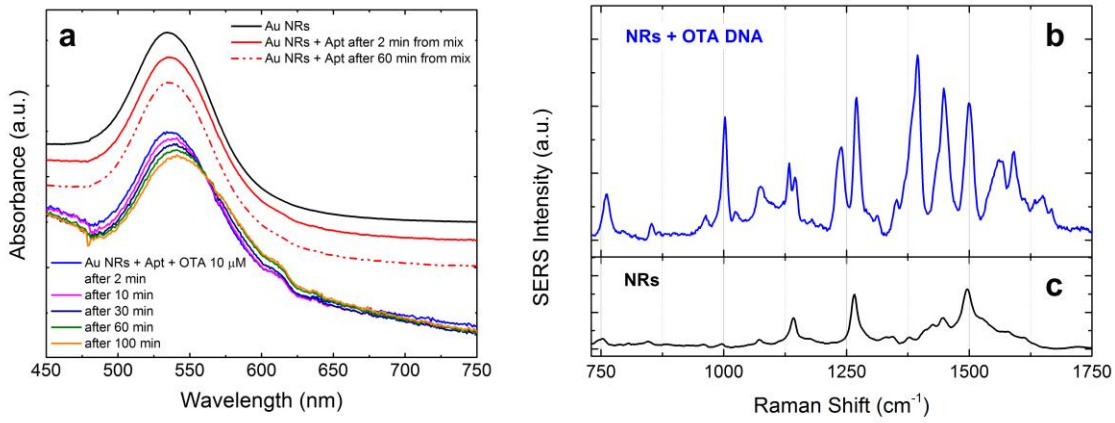

Figure 11 – (a) Extinction spectra of CTAB-coated gold NRs (black line) Vs aptamers-functionalized NRs after 2 min (red solid line) and 60 min (red dashed line). The functionalization induces a red-shift of 2 nm that does not change with time. Addition of OTA (10 μM) causes a progressive shift and broadening of the NRs LSPR (colored spectra in the bottom part of the figure), as a consequence of the interaction between aptamers and OTA molecules. (b) SERS signal of the DNA aptamers for OTA from the functionalized NRs aggregated at the bottom of the glass microcell (P = 5 mW T = 1s).

Peer-reviewed version available at Materials 2018, 11, 440; doi:10.3390/ma11030440

SERS signal was averaged over 100 consecutive spectra. (c) Reference CTAB SERS spectrum acquired from aggregates at the bottom of the glass microcell (P = 1.8 mW T =1 s) in absence of biomolecules.

Upon mixing functionalized NRs with Ochratoxin 10 μM and waiting for an incubation time of about one hour it has been possible to induce optical aggregation with 5 mW laser power after few minutes of laser irradiation of the sample with integration times ranging from 1 s to 10 s. The averaged spectrum for Ochratoxin 10 μM and 1 μM are displayed in Figure 12 (blue and red lines). The dashed boxes highlight the zones in which the spectra differ from the SERS of ssDNA. Main differences are observed from 1520 to 1670 cm^{-1} and they can be attributed to the vibrational modes of the amide group present in OTA molecular structure [57]. Other bands due to OTA molecules are seen at 1310 cm^{-1} (stretching of aromatic rings), at 1130 and 1160 cm^{-1} (C-N ring stretching). Further evidences that aptamers captured OTA molecules can be found in the modification of the relative intensity of some vibrational modes of the ssDNA, such as the stronger intensity of the ring stretching of guanine at 1395 cm^{-1} with respect the band at 1450 cm^{-1}, or the intensity of the peak at 1424 cm^{-1} due to the H-bond deformation of Deoxyribosyl (C5'), which indeed increases with OTA concentration [57].

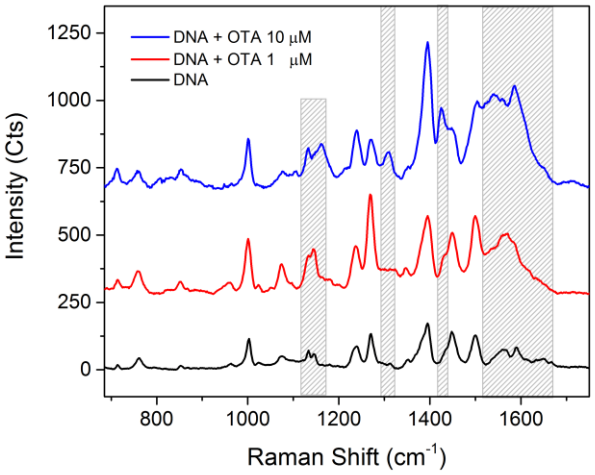

Figure 12 – LIQUISOR SERS spectrum of DNA aptamers for OTA (black line – P = 5 mW T = 1s) compared with the SERS spectrum observed from induced aggregates formed by functionalized NRs mixed with OTA 10 μM (blue line – P = 5 mW T = 1s) and 1 μM (red line – P = 5 mW T = 1s). Dashed boxes highlight the spectral regions where the most evident differences can be observed. All the SERS spectra are averaged over at least 100 consecutive spectra. Data are offset for clarity.

4. Conclusions

The LIQUISOR exploits optical forces to aggregate metal nanoparticles in presence of molecular compounds solutions and induce strong SERS signals that can be used for high sensitivity molecular detection in liquid environment. In this work we have applied the LIQUISOR to detect hemeproteins (Hgb and Cat). Detection at physiological pH has been demonstrated, reaching sensitivities of few ng/mL (pM) for Hgb and of few μg/mL (10 nM) for Cat. Working on BSA, we have studied the growth kinetics of optically induced aggregates, reaching a detection limit of 50 nM and showing a monotonic signal increase with the concentration that paves the way to quantitative applications of the LIQUISOR methodology. A model has been developed that describes the process of nanorod/protein binding and size increase of the BIO-NRCs, supported by the experimental results. Finally, we have carried out first experiments on the LIQUISOR detection of Ochratoxin A exploiting nanorods functionalized with specific DNA aptamers. Aptamers have shown the capability to efficiently capture toxins in solutions and yield strong SERS. These experiments represent a first step towards the addition of molecular specificity to the LIQUISOR concept.

LIQUISOR is of rapid use (few minutes), experimentally simple (standard micro-spectrometers and commercial nanorods are used) and intrinsically scalable to lab-on-chip devices. Several possible developments are envisaged for this technique such as: the use of more efficient nanostructures (e.g. core-shell, gold-silver alloys, nanostars) [93,94,95,96] to improve the limit of detection; the exploration of new configurations for specific detection (e.g. employing functionalized surfaces to increase the affinity between BIO-NRCs and substrates); the integration in micro-fluidic chips; the use of laser beams in the optical transparency window of biological tissues that could enable the application of our scheme in combination with optical injection of nanoparticles into living cells for *in-vivo* detection.

Supplementary Materials: The following are available online at www.mdpi.com/link, Figure S1: LSPR spectrum of the NRs. Figure S2: Plot of the optical forces acting on the NRs. Figure S3: Fits of the LSPR profiles of individual and aggregated NRs. Figure S4: SERS intensity at saturation of different characteristic Raman modes of BSA. Table S1: Best fit parameters (exponent) of the data in Figure S2, Table S2: Position of the vibrational modes of Hgb measured in PBS solution (0.1 mM), in powder state and through the LIQUISOR method (10 μM).

Acknowledgments: We acknowledge the financial support from the project COST MP1302 Nanospectroscopy through its STSM program, MIUR PON02_00355_2964193-Hippocrates "Sviluppo di Micro e Nano-Tecnologie e Sistemi Avanzati per la Salute dell'uomo", the CNR Short Term Mobility program, ANR P2N PIRANEX (ANR-12-NANO-0016), French Government and ANRT Association Nationale de la Recherche et de la Technologie.

Author Contributions: A.F. carried out the SERS measurements, the data analysis and the optical patterning experiments; C.d'A. contributed to the systematic SERS measurements on BSA; B.F. carried out the LSPR measurements; V.V. and N.M. carried out and analyzed the DLS measurements; M.G.D. and O.M.M. carried out the optical forces calculations; R.G. carried out the functionalization of the nanoparticles; M.L. provided the materials and supervised the experiments on the toxins; A.F. and P.G.G. wrote the paper; P.G.G. conceived the experiment and supervised the research. All authors discussed and commented on the manuscript.

Conflicts of Interest: "The authors declare no conflict of interest."

747 **References**

1 Le Ru, E.; Etchegoin, P.G. *Principles of Surface Enhanced Raman Spectroscopy*. Elsevier, 2009, ISBN: 978-0-444-52779-0.

2 Schluecker, S. Surface-Enhanced Raman Spectroscopy: Concepts and Chemical Applications. *Ang. Chem. Int. Ed.* **2014**, 53, 4756-4795, DOI: 10.1002/anie.201205748

3 Han, X.X.; Huang, G.G.; Zhao, B.; Ozaki, Y. Label-free highly sensitive detection of proteins in aqueous solutions using surface-enhanced Raman scattering. *Anal. Chem.* **2009**, 81, 3329–33, DOI: 10.1021/ac900395x.

4 Yang, X.; Gu, C.; Qian, F.; Li, Y.; Zhang, Y.L. Highly sensitive detection of proteins and bacteria in aqueous solution using surface-enhanced Raman scattering and optical fibers. *Anal. Chem.* **2011**, 83, 5888–94, DOI: 10.1021/ac200707t.

5 Schluecker, S. SERS Microscopy: Nanoparticle Probes and Biomedical Applications. *CHEMPHYSCHEM* **2009**, 10, 1344-1354, DOI: 10.1002/cphc.200900119

6 Maier, S.A. *Plasmonics: Fundamentals and applications*. New York, NY: Springer Verlag, 2007, ISBN: 978-0-387-37825-1.

7 Amendola, V.; Pilot, R.; Frasconi, M.; Maragò, O.M.; Iatì, A. Surface plasmon resonance in gold nanoparticles: a review. *J. Phys. Condens. Matter*. **2017**, 29, 203002, DOI: 10.1088/1361-648X/aa60f3.

8 Kneipp, K.; Haka, A.S.; Kneipp, H.; Badizadegan, K.; Yoshizawa, N.; Boone, C.; Shafer-Peltier, K.E.; Motz, J.T.; Dasari, R.R.; Feld, M.S. Surface-Enhanced Raman Spectroscopy in Single Living Cells Using Gold Nanoparticles. *Appl. Spectrosc.* **2002**, 56, 150, DOI: https://doi.org/10.1366/0003702021954557.

9 Feng, M.; Tachikawa, H. Surface-enhanced resonance Raman spectroscopic characterization of the protein native structure. *J. Am. Chem. Soc.* **2008**, 130, 7443-7448, DOI: 10.1021/ja8006337.

10 Xu, L.J.; Zong, C.; Zheng, X.-S.; Hu, P.; Feng, J.-M.; Ren, B. Label free detection of Native proteins by surface enhanced Raman spectroscopy Using iodide modified Nanoparticles. *Anal. Chem.* **2014**, 86, 2238-45, DOI: 10.1021/ac403974n.

11 Amendola V.; Meneghetti M. Laser ablation synthesis in solution and size manipulation of noble metal nanoparticles. *Phys. Chem. Chem. Phys.* **2009**, 11, 3805–3821, DOI: 10.1039/b900654k.

12 Zakel, S.; Rienitz, O.; Güttler, B.; Stosch, R. Double isotope dilution surface-enhanced Raman scattering as a reference procedure for the quantification of biomarkers in human serum. *Analyst* **2011**, 136, 3956–3961, DOI: 10.1039/C1AN15207F.

13 Kessentini S.; Barchiesi, D.; D'Andrea, C.; Toma, A.; Guillot, N.; Di Fabrizio, E.; Fazio, B.; Maragò, O.M.; Gucciardi, P.G.; Lamy de la Chapelle, M. Gold Dimer Nanoantenna with Slanted Gap for Tunable LSPR and Improved SERS. *J. Phys. Chem. C* **2014**, 118, 6, 3209–3219, DOI: 10.1021/jp409844y.

14 Liu, H.L.; Yang, Z.; Meng, L.; Sun, Y.; Wang, J.; Yang, L.; Liu, J.; Tian, Z. Three-dimensional and time-ordered surface-enhanced Raman scattering hotspot matrix. *J. Am. Chem. Soc.* **2014**, 136, 5332–5341, DOI: 10.1021/ja501951v.

15 Savage, K.; Hawkeye, M.M.; Esteban, R.; Borisov, A.G.; Aizpurua, J.; Baumberg, J.J. Revealing the quantum regime in tunnelling plasmonics. *Nature* **2012**, 491, 574, DOI: 10.1038/nature11653.

16 Zhu, W.; Crozier, K.B. Quantum mechanical limit to plasmonic enhancement as observed by surface enhanced Raman scattering. *Nat. Commun.* **2014**, 5, DOI: 10.1038/ncomms6228.

17 De Angelis, F.; Gentile, F.; Mecarini, F.; Das, G.; Moretti, M.; Candeloro, P.; Coluccio, M.L.; Cojoc, G.; Accardo, A.; Liberale, C.; Zaccaria, R.P.; Perozziello, G.; Tirinato, L.; Toma, A.; Cuda, G.; Cingolani, R.; Di Fabrizio, E. Breaking the diffusion limit with super-hydrophobic delivery of molecules to plasmonic nanofocusing SERS structures. *Nat. Photonics* **2011**, 5, 682, DOI: 10.1038/nphoton.2011.222.

18 Yang, S.; *et al.* Ultrasensitive surface-enhanced Raman scattering detection in common fluids. PNAS **2016**, 113, 268–273.

19 Jana, N.R. Silver coated gold nanoparticles as new surface enhanced Raman substrate at low analyte concentration. *Analyst* **2003**, 128, 954–56, DOI: 10.1039/B302409A.

20 Messina, E.; Cavallaro, E.; Cacciola, A.; Saija, R.; Borghese, F.; Denti, P.; Fazio, B.; D'Andrea, C.; Gucciardi, P.G.; Iatì, A.M.; Meneghetti, M.; Compagnini, G.; Amendola, V.; Maragò, O.M. Manipulation and Raman Spectroscopy with Optically Trapped Metal Nanoparticles Obtained by Pulsed Laser Ablation in Liquids. *J. Phys. Chem. C* **2011**, 115, 5115–5122, DOI: 10.1021/jp109405j.

21 Sivanesan, A.; Ly, H.K.; Kozuch, J.; Sezer, M.; Kuhlmann, U.; Fisher, A.; Weidinger, I.M. Functionalized Ag nanoparticles with tunable optical properties for selective protein analysis. *Chem. Commun.* **2011**, 47, 3553–5, DOI: 10.1039/C0CC05058J.

22 Bjerneld, E.J.; Svedberg, F.; Käll, M. Laser-Induced Growth and Deposition of Noble-Metal Nanoparticles for Surface-Enhanced Raman Scattering. *Nano Lett.* **2003**, 3, 593-6, DOI: 10.1021/nl034034r.

23 Lee, S.J.; Piorek, B.D.; Meinhart, C.D.; Moskovits, M. Photoreduction at a Distance: Facile, Nonlocal Photoreduction of Ag Ions in solution by Plasmon-Mediated Photoemitted Electrons, *Nano Lett.* **2010**, 10, 1329-34, DOI: 10.1021/nl904173f.

24 Toussaint, K.C.; Liu, M.; Pelton, M.; Pesic, J.; Guffey, M.J.; Guyot-Sionnest, P.; Scherer, N.F. Plasmon resonance based optical trapping of single and multiple Au NPs. *Opt. Express* **2007**, 15, 19, 12018, DOI: https://doi.org/10.1364/OE.15.012017.

25 Liu, Y.; Huang, Z.; Zhou, F.; Lei, X.; Yao, B.; Meng, G.; Mao, Q. Highly sensitive fibre surface enhanced Raman scattering probes fabricated using laser induced self assembly in a meniscus, *Nanoscale* **2016**, 8, 10607-14, DOI: 10.1039/C5NR06773A.

26 Lin, L.; Peng, X.; Wang, M.; Scarabelli, L.; Mao, Z.; Liz-Marzán, L.M.; Becker, M.F.; Zheng, Y. Light-directed reversible assembly of plasmonic nanoparticles using plasmon-enhanced thermophoresis, *ACS Nano* **2016**, 10, 9659-68, DOI: 10.1021/acsnano.6b05486.

27 Ding, T.; Valev, V.K.; Salmon, A.R.; Forman, C.J.; Smoukov, S.K.; Scherman, O.A.; Frenkel, D.; Baumberg, J.J. Light-induced actuating nanotransducers, *P. Natl. Acad. Sci. USA* **2016**, 113, 201524209, DOI: 10.1073/pnas.1524209113.

28 Baffou, G.; Quidant, R. Thermo-plasmonics: using metallic nanostructures as nano-sources of heat. *Laser Photonics Rev.* **2013**, 7, 171–87, DOI: 10.1002/lpor.201200003.

29 Ashkin, A. Acceleration and trapping of particles by radiation pressure. *Phys. Rev. Lett.* **1970**, 24, 156, DOI: https://doi.org/10.1103/PhysRevLett.24.156.

30 Jones, P.; Maragó O.M.; Volpe G., *Optical tweezers: Principles and applications*. Cambridge University Press, 2015, ISBN: 9781107279711.

31 Svedberg, F.; Käll, M. On the importance of optical forces in surface-enhanced Raman scattering (SERS). *Faraday Discuss*. **2006**, 132, 35–44, DOI: 10.1039/B509301P.

32 Maragò, O.M.; Jones, P.H.; Gucciardi, P.G.; Volpe, G.; Ferrari, A.C. Optical trapping and manipulation of nanostructures. *Nat. Nanotechnol.* **2013**, 8, 807–819, DOI: 10.1038/nnano.2013.208.

33 Messina, E.; Cavallaro, E.; Cacciola, A.; Iatì, M.A.; Gucciardi, P.G.; Borghese, F.; Denti, P.; Saija, R.; Compagnini, G.; Meneghetti, M.; Amendola, V.; Maragò, O.M. Plasmon-enhanced optical trapping of gold nanoaggregates with selected optical properties. *ACS Nano* **2011**, 5, 905–913, DOI: 10.1021/nn102101a.

34 Patra, P.P.; Chikkaraddy, R.; Tripathi, R.P.N.; Dasgupta, A.; Kumar, P.G.V. Plasmofluidic single-molecule surface-enhanced Raman scattering from dynamic assembly of plasmonic nanoparticles. *Nat. Commun.* **2014**, 5, 4357, DOI: 10.1038/ncomms5357.

35 Li, M.; Lohmueller, T.; Feldmann, J. Optical Injection of Gold Nanoparticles into Living Cells, *Nano Lett.* **2015**, 15, 770-775, DOI: 10.1021/nl504497m.

36 Arias-González, J.R.; Nieto-Vesperinas M. Optical forces on small particles: attractive and repulsive nature and plasmon-resonance conditions. *J. Opt. Soc. Am. A,* **2003**, 20, 1201–1209, DOI: https://doi.org/10.1364/JOSAA.20.001201.

37 Selhuber-Unkel, C.; Zins, I.; Schubert, O.; Sönnichsen, C.; Oddershede, L.B. Quantitative optical trapping of single gold nanorods. *Nano Lett.* **2008**, 8, 2998–3003, DOI: 10.1021/nl802053h.

38 Brzobohatý, O.; Šiler, M.; Trojek, J.; Chvátal, L.; Karásek, V.; Paták, A.; Pokorná, Z.; Mika, F.; Zemánek, P. Three-dimensional optical trapping of a plasmonic nanoparticle using low numerical aperture optical tweezers. *Sci. Rep. UK* **2015**, 5, 8106, DOI: 10.1038/srep08106.

39 Guffey, M.J.; Scherer, N.F. All-optical patterning of Au nanoparticles on surfaces using optical traps. *Nano Lett.* **2010**, 10, 4302–4308, DOI: 10.1021/nl904167t.

40 Gargiulo, J.; Violi, I.L.; Cerrota, S.; Chvátal, L.; Cortés, E.; Perassi, E.M.; Diaz, F.; Zemánek, P.; Stefani, F.D. Accuracy and Mechanistic Details of Optical Printing of Single Au and Ag Nanoparticles. *ACS Nano* **2017**, 11, 10, 9678–9688, DOI: 10.1021/acsnano.7b04136

41 Svedberg, F.; Li, Z.; Xu, H.; Käll, M. Creating hot nanoparticle pairs for surface-enhanced Raman spectroscopy through optical manipulation. *Nano Lett*. **2006**, 6, 2639–41, DOI: 10.1021/nl062101m.

42 Tanaka, Y.; Yoshikawa, H.; Itoh, T.; Ishikawa, M. Surface Enhanced Raman Scattering from Pseudoisocyanine on Ag Nanoaggregates Produced by Optical Trapping with a Linearly Polarized Laser Beam. *J. Phys. Chem. C* **2009**, 113, 11856, DOI: 10.1021/jp901972m.

43 Bálint, S.; Kreuzer, M.P.; Rao, S.; Badenes, G.; Miškovský, P.; Petrov, D. Simple route for preparing optically trappable probes for surface-enhanced Raman scattering. *J. Phys. Chem. C* **2009**, 113, 17724–9, DOI: 10.1021/jp906318n.

44 Liu, Z.; Hung, W.H.; Aykol, M.; Valley, D.; Cronin, S.B. Optical manipulation of plasmonic nanoparticles, bubble formation and patterning of SERS aggregates. *Nanotechnology* **2010**, 21, 105304, DOI: https://doi.org/10.1088/0957-4484/21/10/105304.

45 Tong, T.; Righini, M.; Gonzalez, M.U.; Quidant, R.; Käll, M. Optical aggregation of metal nanoparticles in a microfluidic channel for surface-enhanced Raman scattering analysis. *Lab. Chip.* **2009**, 9, 193-5, DOI: 10.1039/B813204F.

46 Fazio, B.; D'Andrea, C.; Foti, A.; Messina, E.; Irrera, A.; Donato, M.G.; Villari, V.; Micali, N.; Maragò, O.M.; Gucciardi, P.G. SERS detection of Biomolecules at Physiological pH via aggregation of Gold Nanorods mediated by Optical Forces and Plasmonic Heating, *Sci. Rep. UK* **2016**, 6, 26952, DOI: 10.1038/srep26952.

47 Guttler, Bernd, Zackel, S.; Wundrack, S.; Stosch, R. Isotope-Dilution Surface-Enhanced Raman Spectroscopy: Metrologically Traceable Reference Measurements at the Highest Precision Level and Their Application in Clinical Chemistry. In *Handbook of Enhanced Spectroscopy*, Pan Stanford Publishing Pte. Ltd, 2016; pp. 307-328, ISBN: 9789814613323.

48 Maerz, A.K.; Ackermann, R.; Malsch, D.; Bocklitz, Th.; Henkel, Th.; Popp, J. Towards a quantitative SERS approach – online monitoring of analytes in a microfluidic system with isotope-edited internal standards. *J. Biophotonics* **2009**, 2, 232, DOI: 10.1002/jbio.200810069.

49 Shen, W.; Lin, X.; Jiang, C.; Li, C.; Lin, H.; Huang, J.; Wang, S.; Liu, G.; Yan, X.; Zhong, Q.; Ren, B. Reliable quantitative SERS analysis facilitated by core–shell nanoparticles with embedded internal standards. *Angew. Chem. Int. Edit.* **2015**, 54, 25, 7308-7312, DOI: 10.1002/anie.201502171.

50 Nima, Z.; Mahmood, M.; Xu, Y.; Mustafa, T.; Watanabe, F.; Nedosekin, D.A.; Juratli, M.A.; Fahmi, T.; Galanzha, E.I.; Nolan, J.P.; Basnakian, A.G.; Zharov, V.P.; Biris, A.S. Circulating tumor cell identification by functionalized silver-gold nanorods with multicolor, super-enhanced SERS and photothermal resonances, *Sci. Rep. UK* **2014**, 4, 4752, DOI: 10.1038/srep04752.

51 Tombelli, S.; Minunni, M.; Mascini, M. Analytical Applications of Aptamers. *Biosens. Bioelectron.* **2005**, 20, 2424−2434, DOI: https://doi.org/10.1016/j.bios.2004.11.006.

52 Fabris, L.; Dante, M.; Nguyen, T.-Q.; Tok, J.B.-H.; Bazan, G.C. SERS Aptatags: New Responsive Metallic Nanostructures for Heterogeneous Protein Detection by Surface Enhanced Raman Spectroscopy, *Adv. Funct. Mater*. **2008**, 18, 2518–2525, DOI: 10.1002/adfm.200800301.

53 O'sullivan, C.K.; Guilbault, G.G. Commercial Quartz Crystal Microbalances−Theory and Applications. *Biosens. Bioelectron*. **1999**, 14, 663−670, DOI: https://doi.org/10.1016/S0956-5663(99)00040-8.

54 Lequin, R.M. Enzyme Immunoassay (Eia)/Enzyme-Linked Immunosorbent Assay (Elisa). *Clin. Chem.* **2005**, 51, 2415−2418, DOI: https://doi.org/10.1373/clinchem.2005.051532.

55 Hoa, X.D.; Kirk, A.G., Tabrizian, M. Towards integrated and sensitive surface plasmon resonance biosensors: A review of recent progress. *Biosens. Bioelectron.* **2007**, 23, 151–160, DOI: https://doi.org/10.1016/j.bios.2007.07.001.

56 Cottat, M.; D'Andrea, C.; Yasukuni, R.; Malashikhina, N.; Grinyte, R.; Lidgi-Guigui, N.; Fazio, B.; Sutton, A.; Oudar, O.; Charnaux, N.; Pavlov, V.; Toma, A.; Di Fabrizio, E.; Gucciardi, P.G., Lamy de la Chapelle, M. High Sensitivity, High Selectivity SERS Detection of MnSOD Using Optical Nanoantennas Functionalized with Aptamers, *J. Phys. Chem. C* **2015**, 119, 15532−15540, DOI: 10.1021/acs.jpcc.5b03681.

57 Galarreta, B.C.; Tabatabaei, M.; Guieu, V.; Peyrin, E.; Lagugné-Labarthet, F. Microfluidic channel with embedded SERS 2D platform for the aptamer detection of ochratoxin A, *Anal. Bioanal. Chem.* **2013**, 405, 1613–1621, DOI: 10.1007/s00216-012-6557-7.

58 Neumann, O.; Zhang, D.; Tam, F.; Lai, S.; Wittung-Stafshede, P.; Halas, N.J. Direct Optical Detection of Aptamer Conformational Changes Induced by Target Molecules, *Anal. Chem.* **2009**, 81, 10002–10006, DOI: 10.1021/ac901849k.

59 Cruz-Aguado, J. A.; Penner, G. Fluorescence Polarization Based Displacement Assay for the Determination of Small Molecules with Aptamers. *Anal. Chem.* **2008**, 80, 8853–8855, DOI: 10.1021/ac8017058.

60 Villari, V.; Mazzaglia, A.; Darcy, R.; O'Driscoll, C. M.; Micali, N. Nanostructures of Cationic Amphiphilic Cyclodextrin Complexes with DNA, *Biomacromolecules* **2013**, 14, 811−817, DOI: 10.1021/bm3018609.

61 D'Andrea, C.; Irrera, A.; Fazio, B.; Foti, A.; Messina, E.; Maragò, O. M.; Kessentini, S.; David, C.; Gucciardi, P. G. Red shifted spectral dependence of the SERS enhancement in a random array of gold nanoparticles covered with a silica shell: extinction versus scattering, *J. Optics* **2015**, 17, 114016, DOI: 10.1088/2040-8978/17/11/114016

62 Shemetov, A.A.; Nabiev, I.; Sukhanova, A. Molecular interaction of proteins and peptides with nanoparticles, *ACS Nano* **2012**, 6, 4585-4602, DOI: 10.1021/nn300415x.

63 Kah, J.C.Y.; Zubieta, A.; Saavedra, R.A.; Hamad-Schifferli, K. Stability of Gold Nanorods Passivated with Amphiphilic Ligands. *Langmuir* **2012**, 28, 8834–8844, DOI: 10.1021/la3000944.

64 Tsai, D.H.; Del Rio, F.W.; Keene, A.M.; Tyner, K.M.; Mac Cuspie, R.I.; Cho, T.J.; Zachariah, M.R.; Hackley, V.A. Adsorption and Conformation of Serum Albumin Protein on Gold Nanoparticles Investigated Using Dimensional Measurements and in Situ Spectroscopic Methods, *Langmuir* **2011**, 27, 6, 2464, DOI: 10.1021/la104124d.

65 Wang, L.; Li, J.; Pan, J.; Jiang, X.; Ji, Y.; Li, Y.; Qu, Y.; Zhao, Y.; Wu, X.; Chen, C. Revealing the Binding Structure of the Protein Corona on Gold Nanorods Using Synchrotron Radiation-Based Techniques: Understanding the Reduced Damage in Cell Membranes, *J. Am. Chem. Soc.* **2013**, 135, 17359−17368, DOI: 10.1021/ja406924v.

66 Zijlstra, P.; Pedro, M.R.P.; Orrit. M. Optical detection of single non-absorbing molecules using the surface plasmon resonance of a gold nanorod. *Nat. Nanotechnol.* **2012**, **7,** 379–382, DOI: 10.1038/nnano.2012.51.

67 Zhang, D.; Neumann, O.; Wang, H.; Yuwono, V.M.; Barhoumi, A.; Perham, M.; Hartgerink, J.D.; Wittung-Stafshede, P.; Halas, N.J. Gold Nanoparticles Can Induce the Formation of Protein-based Aggregates at Physiological pH, *Nano Lett.* **2009**, 9, 2, 666-671, DOI: 10.1021/nl803054h.

68 Dubois, L.H.; Nuzzo, R.G.; Synthesis, structure, and properties of model organic surfaces, *Annu. Rev. Phys. Chem.* **1992**, 43, 437.

69 Thioune, N.; Lidgi-Guigui, N.; Cottat, M.; Gabudean, A.M.; Focsan, M.; Benoist, H.M.; Astilean, S.; Lamy de la Chapelle, M. Study of gold nanorods–protein interaction by localized surface plasmon resonance spectroscopy. *Gold Bull.* **2013**, 46, 275, 2013, DOI: 10.1007/s13404-013-0118-5.

70 Sheehan, P.E.; Whitman, L.J. Detection Limits for Nanoscale Biosensors, *Nano Lett.*, **2005**, 5, 4, 803-807, DOI: 10.1021/nl050298x.

71 Donato, MG; Messina, E; Foti, A; Smart, T; Jones, PH; Iatì, MA; Saija, R; Gucciardi, PG; Maragò, OM. Optical trapping and optical force positioning of two- dimensional materials. *Nanoscale*, **2018,** DOI: 10.1039/C7NR06465A

72 Zhao, Y; Sun, M; Ma, W; Kuang, H. Xu, C. Biological Molecules-Governed Plasmonic Nanoparticle Dimers with Tailored Optical Behaviors, *J. Phys. Chem. Lett.*, **2017**, 8, 5633, DOI: 10.1021/acs.jpclett.7b01781

73 Novotny, L.; Hecht B. *Principles of Nano-optics*, 2nd Ed., Cambridge University Press, Cambridge, 2012, ISBN: 978-1-107-00546-4.

74 Lehninger A.L. *Biochemistry*, 2nd Ed.; Worth Publishers, Inc., New York, 1975; p. 111, ISBN: 978-0879010478.

75 De Luca, A.C.; Rusciano, G.; Ciancia, R.; Martinelli, V.; Pesce, G.; Rotoli, B.; Selvaggi, L.; Sasso, A. Spectroscopical and mechanical characterization of normal and thalassemic red blood cells by Raman Tweezers, *Opt. Express* **2008**, 16, 11 7943–7957, DOI: https://doi.org/10.1364/OE.16.007943.

76 Brunner, H.; Sussner H. Resonance Raman scattering on haemoglobin, *Biochim. Biophys Acta* **1973**, 310, 20-31, DOI: https://doi.org/10.1016/0005-2795(73)90004-4.

77 Xu, H.; Bjerneld, E.J.; Käll, M.; Börjesson, L. Spectroscopy of Single Hemoglobin Molecules by Surface Enhanced Raman Scattering, *Phys. Rev. Lett.* **1999**, 83, 21, 4357-4360, DOI: https://doi.org/10.1103/PhysRevLett.83.4357.

78 Drescher, D.; Büchner, T.; McNaughton, D.; Kneipp, J. SERS reveals the specific interaction of silver and gold nanoparticles with hemoglobin and red blood cell components. Phys. Chem. Chem. Phys. **2013**, 15, 5364, DOI: 10.1039/C3CP43883J.

79 Kaminska, A.; Forster, R.J.; Kayes, T.E. The impact of adsorption of bovine pancreatic trypsin inhibitor on CTAB-protected gold nanoparticle arrays: a Raman spectroscopic comparison with solution denaturation. *J. Raman Spectrosc.* **2010**, 41, 130–135, DOI: 10.1002/jrs.2477.

80 Dendramis, A.L.; Schwinn, E.W.; Sperline, R.P. SERS study of CTAB on Copper, *Surf. Sci.* **1983**, 134, 675-688, DOI: https://doi.org/10.1016/0039-6028(83)90065-1.

81 Khan, S.; Gupta, A.; Verma, N.C.; Nandi, C.K. Kinetics of protein adsorption on gold nanoparticle with variable protein structure and nanoparticle size. *J. Chem. Phys.* **2015**, 143, 164709, DOI: https://doi.org/10.1063/1.4934605.

82 Bergmeyer, H. U. Methods of Enzymatic Analysis, 2nd ed., Vol. I, ed., 438-439, Academic Press, New York, (NY: 1974).

83 Sánchez-Rodríguez, R.; Torres-Mena, J.E.; del Pozo Yauner, L.; Pérez-Carreón, J.I. *Biomarkers of the Antioxidant Response: A Focus on Liver Carcinogenesis in Biomarkers in Liver Disease*, Springer Netherlands, 2016; pp 1-24, ISBN: 978-94-007-7742-2.

84 Vlahogianni, T.; Dassenakis, M.; Scoullos, M.J.; Valavanidis, A.; Integrated use of biomarkers (superoxide dismutase, catalase and lipid peroxidation) in mussels *Mytilus galloprovincialis* for assessing heavy metals' pollution in coastal areas from the Saronikos Gulf of Greece, *Mar. Pollut. Bull.* **2007**, 54, 1361–1371, DOI: https://doi.org/10.1016/j.marpolbul.2007.05.018.

85 Chuang, W.-J.; Johnson, S.; Van Wart, H.E. Resonance Raman Spectra of Bovine Liver Catalase: Enhancement of Proximal Tyrosinate Vibrations, *J. Inorg. Biochem*. **1988**, 34,201-219, DOI: https://doi.org/10.1016/0162-0134(88)85030-X.

86 Zezza, F.; Longobardi F.; Pascale, M.; Eremin, S.A.; Visconti, A. Fluorescence polarization immunoassay for rapid screening of ochratoxin A in red wine, *Anal. Bioanal. Chem.* **2009**, 395, 1317–1323, DOI: https://doi.org/10.1007/s00216-009-2994-3.

87 Kabak, B. Ochratoxin A in cereal-derived products in Turkey: occurrence and exposure assessment, *Food Chem. Toxicol.* **2009**, 47, 348–352, DOI: https://doi.org/10.1016/j.fct.2008.11.019.

88 O'Brien, E.; Dietrich, D.R.; Ochratoxin A: the continuing enigma, *Crit. Rev. Toxicol*. **2005**, 35, 33–60, DOI: http://dx.doi.org/10.1080/10408440590905948.

89 Ganbold, E.-O.; Lee, C.M.; Cho, E.-M.; Son, S.J.; Kim, S.; Joo, S.-W., Yang, S.I. Subnanomolar detection of ochratoxin A using aptamer-attached silver nanoparticles and surface-enhanced Raman scattering, *Anal. Methods UK* **2014**, 6, 3573, DOI: 10.1039/C4AY00440J.

90 Gillibert, G.; Triba, M.; Lamy de la Chapelle, M. Surface Enhanced Raman Scattering Sensor for Highly Sensitive and Selective Detection of Ochratoxin A, *Analyst* **2018**, 143, 339, DOI: 10.1039/C7AN01730H.

91 Indrasekara, A.; Wadams, R.; Fabris, L. Ligand Exchange on Gold Nanorods: Going Back to the Future, *Part. Part. Syst. Charact.* **2014**, 31, 819–838, DOI: 10.1002/ppsc.201400006.

92 Le Ru, E.C.; Grand, J.; Sow, I.; Somerville, W.R.C.; Etchegoin, P.G.; Treguer-Delapierre, M.; Charron, G.; Félidj, N.; Lévi, G.; Aubard, J. A Scheme for Detecting Every Single Target Molecule with Surface-Enhanced Raman Spectroscopy, *Nano Lett.* **2011**, 11, 5013–5019, DOI: 10.1021/nl2030344.

93 Messina, E.; Donato, M.G.; Zimbone, M.; Saija, R.; Iatì, M.A.; Calcagno, L.; Fragalà, M.E.; Compagnini, G.; D'Andrea, C.; Foti, A.; Gucciardi, P.G.; Maragò, O.M. Optical trapping of silver nanoplatelets, *Opt. express* **2015**, 23, 8720-8730, DOI: https://doi.org/10.1364/OE.23.008720.

94 Schutz, M.; Steinigeweg, D.; Salehi, M.; Kompe, K.; Schlucker, S. Hydrophilically stabilized gold nanostars as SERS labels for tissue imaging of the tumor suppressor p63 by immuno-SERS microscopy. *Chem. Commun.* **47**, 4216-4218, DOI: 10.1039/c0cc05229a.

95 Messina, E.; D'Urso, L.; Fazio, E.; Satriano, C.; Donato, M.G.; D'Andrea, C.; Maragò, O. M.; Gucciardi, P.G.; Compagnini, G.; Neri, F. Tuning the structural and optical properties of gold/silver nano-alloys prepared by laser ablation in liquids for optical limiting, ultra-sensitive spectroscopy, and optical trapping. *J. Quant. Spectrosc. Rad. Trans.* **2012**, 113, 220-228, DOI: 10.1016/j.jqsrt.2012.06.023

96 Spadaro, D.; Iatí, M.A.; Pérez-Piñeiro, J.; Vázquez-Vázquez, J.; Correa-Duarte, M.A.; Donato, M.G.; Gucciardi, P.G.; Raija, R.; Strangi, G.; Maragò, O.M. Optical Trapping of Plasmonic Mesocapsules: Enhanced Optical Forces and SERS. *J. Phys. Chem. C* **2017**, 121, 691-700, DOI: 10.1021/acs.jpcc.6b10213.